

ADAPTIVE CONSTRAINT INTEGRATION FOR SIMULTANEOUSLY OPTIMIZING CRYSTAL STRUCTURES WITH MULTIPLE TARGETED PROPERTIES

Anonymous authors

Paper under double-blind review

ABSTRACT

In materials science, finding crystal structures that have targeted properties is crucial. While recent methodologies such as Bayesian optimization and deep generative models have made some advances on this issue, these methods often face difficulties in adaptively incorporating various constraints, such as electrical neutrality and targeted properties optimization, while keeping the desired specific crystal structure. To address these challenges, we have developed the Simultaneous Multi-property Optimization using Adaptive Crystal Synthesizer (SMOACS), which utilizes state-of-the-art property prediction models and their gradients to directly optimize input crystal structures for targeted properties simultaneously. SMOACS enables the integration of adaptive constraints into the optimization process without necessitating model retraining. Thanks to this feature, SMOACS has succeeded in simultaneously optimizing targeted properties while maintaining perovskite structures, even with models trained on diverse crystal types. We have demonstrated the band gap optimization while meeting a challenging constraint, that is, maintaining electrical neutrality in large atomic configurations up to 135 atom sites, where the verification of the electrical neutrality is challenging. The properties of the most promising materials have been confirmed by density functional theory calculations.

1 INTRODUCTION

We address the challenge of simultaneously optimizing multiple material properties while preserving specific crystal structures and ensuring electrical neutrality. To achieve this, we have developed a methodology that leverages property prediction models and their gradients to facilitate the discovery of materials with multiple desired properties. This approach allows for the adaptive application of constraints, such as electrical neutrality and specific crystal structures, without necessitating retraining. As a result, our method enables the optimization of large atomic configurations to obtain specific properties while ensuring electrical neutrality and preserving specific crystal structures.

Materials design is crucial for various advancing technologies, e.g., enhancing efficiency or reducing the cost of solar cells. The goal of materials design is to identify materials that simultaneously satisfy multiple property criteria, for instance, in terms of band gap and formation energy, while meeting other requirements, such as electrical neutrality. Furthermore, during the design process, it is often desirable to focus on specific promising systems, such as perovskite structures for next-generation solar cells (Green et al., 2014). In the exploration of specific crystal structures, elemental substitution—blending different elements—is commonly employed. For instance, blended perovskite structures might have alternative compositions such as $AA'BB'X_2X'X_3''$, which are derived from the standard ABX_3 format of a perovskite unit cell. Computational experiments involving these complex compositions often require larger systems that combine multiple unit cells. Consequently, the critical aspects of material design include 1) the ability to optimize multiple properties simultaneously, 2) the adaptive incorporation of various constraints, such as electrical neutrality or specific crystal structures, and 3) the ability to optimize large atomic configurations. In summary, we need to solve the problem of simultaneously optimizing multiple properties while preserving a specific crystal structure and ensuring electrical neutrality.

Advances in computational techniques have tremendously accelerated material design, with Density Functional Theory (DFT) becoming a standard tool for rapid property validation. Recent developments in machine learning have enabled faster property predictions through deep learning models trained on DFT-generated data. Models such as Crystalformer (Taniai et al., 2024), a transformer-based model (Vaswani et al., 2017), and ALIGNN (Choudhary & DeCost, 2021), a Graph Neural Network (GNN)-based model, significantly facilitate the screening process (Choubisa et al., 2023).

Bayesian optimization, such as Gaussian Process and Tree-structured Parzen estimator (TPE) (Watanabe, 2023), is commonly employed in material design (Ozaki et al., 2020a; Boyar et al., 2024; Zhai et al., 2024). A key advantage of Bayesian optimization is its capability to perform inverse inference, therefore enabling the prediction of crystal structures from given properties. Recently, deep generative models designed to synthesize crystal structures, such as FTCP (Ren et al., 2022), have gained much attention due to their potential to discover new stable materials. Additionally, there are methods that leverage large language models (Ding et al., 2024; Gruver et al., 2024), Generative Flow Networks (AI4Science et al., 2023), reinforcement learning (Govindarajan et al., 2024), or flow matching (Miller et al., 2024) to synthesize new crystal structures.

Despite these advances, many challenges remain. Firstly, research using deep generative models primarily aims to identify stable materials, and only a limited number of studies focus on optimizing both stability and key properties, such as the band gap, which is crucial for maximizing solar cell efficiency. Secondly, deep generative models are often built with specialized architectures, making it difficult to adopt the latest property prediction models for their prediction branches. This lack of flexibility in model architectures can hinder the improvement of prediction accuracy for generated materials. Thirdly, current generative models require retraining for targeted properties optimization within specific crystal structures, which is often the case in practice, such as perovskite structures for solar cells. Finally, verifying the electrical neutrality in large atomic configurations is complicated due to the combinatorial explosion resulting from the possible multiple oxidation numbers for many atomic species. Nevertheless, ensuring electrical neutrality is essential for proposing realistic materials.

To address these challenges, we have developed a framework, the Simultaneous Multi-property Optimization using Adaptive Crystal Synthesizer (SMOACS). SMOACS can employ various property prediction models as far as their gradients can be computed and optimizes input crystal structures directly to achieve target properties through the backpropagation technique (Fig. 1(left)). This approach enables accurate prediction of multiple properties and simultaneous optimization by utilizing several recently developed pre-trained models for predicting different material properties. Unlike methods using normalizing flows that require architectural constraints for invertibility, our method imposes no such restrictions on these models. When newer models become available in the future, improved prediction accuracy will be achieved by incorporating them into our approach. Additionally, by managing the optimization range and utilizing special loss functions, we facilitate targeted properties optimization within specific crystal structures, avoiding retraining. Moreover, by imposing constraints via combinations of oxidation numbers, our method ensures the electrical neutrality of any proposed materials, even in large atomic configurations where verifying electrical neutrality is difficult due to combinatorial explosion. The generalizability of SMOACS enables it to adopt various prediction models and optimize various properties.

SMOACS is the first method that directly optimizes the space of crystal structures using a gradient-based approach. We achieve this by making the entire crystal structure differentiable, which involves decomposing it into various components and representing atomic species as atomic distributions. Unlike traditional methods that convert crystal structures into latent variables (Ren et al., 2022)—thereby entangling their elements—our approach maintains the independence of each component. This independence facilitates the preservation of crystal structures and ensures electrical neutrality by precisely specifying the atoms at each site. Furthermore, unlike generative models that probabilistically generate materials satisfying certain conditions, our method can inherently guarantee electrical neutrality and the preservation of crystal structures. Moreover we can add additional constraints as long as they are differentiable.

We demonstrated that SMOACS could effectively utilize both GNN-based models and transformer-based models, outperforming FTCP, deep generative models, and TPE, Bayesian optimization. We demonstrated the band gap optimization within perovskite structures without retraining, using models trained on the MEGNet dataset (Chen et al., 2019), which includes various types of crystals.

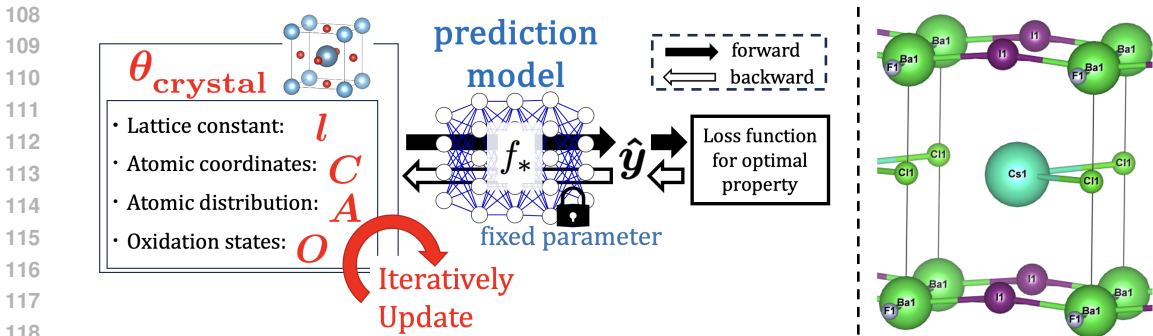


Figure 1: (left) Overview of the SMOACS framework. (right) An example of an optimized perovskite structure with a 4.02 eV band gap, verified at 3.96 eV through DFT calculations. Visualization was done with VESTA (Momma & Izumi, 2011).

Additionally, we demonstrated the optimization for large atomic configurations with as many as 135 atom sites while ensuring electrical neutrality. Furthermore, the validity of the proposed materials was verified through DFT calculations.

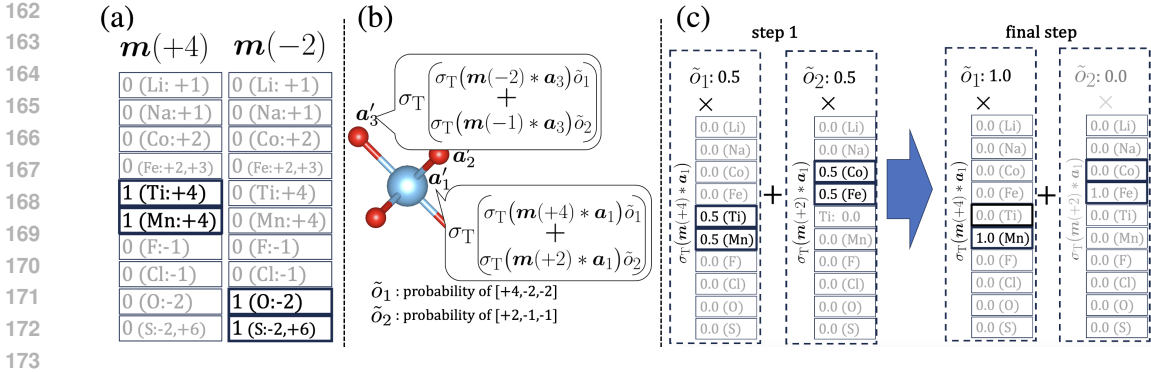
2 RELATED WORKS

Property prediction model. In recent years, much research has actively focused on predicting the properties of materials using DFT-generated data (Davariashtiyani & Kadkhodaei, 2023; Merchant et al., 2023; Yang et al., 2024a). There are two primary approaches involving deep learning. The first approach utilizes GNNs (Chen et al., 2019; Park & Wolverton, 2020; Louis et al., 2020; Schmidt et al., 2021; Lin et al., 2023), such as ALIGNN. The main advantage of using GNNs is their ability to graphically represent crystal structures, thereby considering inter-atomic relationships in more physically meaningful ways. The second approach employs transformers (Ying et al., 2021; Yan et al., 2022), such as Crystalformer, which are known for their promising performance in the field of computer vision and natural language processing (Brown et al., 2020; Dosovitskiy et al., 2021).

Deep generative models. Deep generative models, including language models, for producing new stable materials have been emerging in the last years (Xie et al., 2022; Lyngby & Thygesen, 2022; Sultanov et al., 2023; Yang & Mannodi-Kanakthodi, 2022). However, only a few studies explored material properties and stability at the same time. Studies such as FTCP (Ren et al., 2022), MatterGen (Zeni et al., 2023), and UniMat (Yang et al., 2024b) focused on optimizing properties including band gap and material stability. They are generative models and thus conduct property optimizations within the framework of generative modeling. FTCP, based on Variational Autoencoders (Kingma, 2013), encodes crystal structures into latent variables. It employs prediction branches to predict properties from these variables. MatterGen and UniMat are diffusion models and employ classifier-free guidance (Ho & Salimans, 2021) to generate materials with specific properties. Although methods exist to constrain condition-free models for generating specific outputs (Wu et al., 2024), no research has implemented these techniques for crystal structures.

Bayesian Optimization. Black-box optimization, including Bayesian optimization, is widely used in materials science (Song et al., 2024). Numerous studies in materials science apply Bayesian optimization to predict crystal and molecular structures from target properties (Boyar et al., 2024; Zhai et al., 2024; Khatamsaz et al., 2023). One representative method of Bayesian optimization widely utilized in materials science research is the Gaussian process (GP) (Lu et al., 2022). However, as the Gaussian process only handles continuous values, its ability to manage categorical variables like elements is questionable. The recently proposed Tree-structured Parzen Estimator (TPE), which is capable of handling categorical variables and multi-objective optimization (Ozaki et al., 2020b; 2022) and has been utilized in materials science (Ozaki et al., 2020a), could be a better choice.

Gradient based approach. Gradient-based approaches that aim to optimize design variables toward desired properties using deep learning-based predictors and their gradients have been applied across a wide range of fields. For example, they have been used to optimize designs for dynamics of



174
175
176
177
178
179
180
181
182
183
184
185

Figure 2: (a) SMOACS enforces site-specific restrictions on the types of elements to maintain electrical neutrality. The oxidation masks, labeled $m(+4)$ and $m(-2)$, correspond to elements with oxidation numbers of +4 and -2, respectively. The values 0 and 1 indicate the values of the mask. Parentheses indicate the elements and their potential oxidation numbers at each position. (b) Atomic distributions at each site considering two potential oxidation numbers. Here, we consider two possible patterns of oxidation number combinations: [+4, -2, -2] and [+2, -1, -1] for three sites. The atomic distributions at each site are computed by taking the weighted sum of the probabilities of these patterns. (c) Change in the atomic distribution at site No.1 in the optimization process. The numbers in the grids indicate the probabilities of elements in parentheses. As a result of the optimization, the TiO_2 -type oxidation pattern [+4, -2, -2] is selected, with Mn chosen as the element that achieves a +4 oxidation number.

186
187
188
189
190
191
192

physical systems (Allen et al., 2022; Hwang et al., 2022), image manipulation (Xia et al., 2022), metamaterials (Bordiga et al., 2024), and chemical compositions (Fujii et al., 2024) to achieve target performance. These methods require that the chain rule of differentiation connects from the input to the output. While there is the study that apply this technique by mapping crystal structures into latent spaces (Xie et al., 2022), there are no studies that apply it directly within the space of crystal structures.

193 3 SMOACS

194
195
196
197
198
199

In SMOACS, the crystal structure θ_{crystal} is divided into four learnable parameters: lattice constant l , coordinates of N atomic sites C , elements e , and an oxidation state configuration parameter o (Fig. 1(left)).

$$200 \quad \theta_{\text{crystal}} = \{l, C, e, o\} \quad (1)$$

$$201 \quad l \in \mathbb{R}^6, C \in \mathbb{R}^{N \times 3}, e \in \mathbb{R}^N, o \in \mathbb{R}^D \quad (2)$$

202
203
204
205
206
207
208
209
210
211
212
213
214
215

The lattice constant l comprises the crystallographic axes lengths a, b, c and the angles between these axes α, β, γ . The oxidation state configuration parameter o denotes the probabilities for D patterns of oxidation number combinations determined by initial crystal structures, further described in Section 3.1. The l and C , being continuous variables, can be optimized directly through backpropagation technique (Ren et al., 2020; Fujii et al., 2023). However, this technique cannot be used for the elements e since they are being discrete and categorical. Therefore, instead of directly handling the elements e , we employ a technique where an element at site n is represented by the atomic distribution a_n ($a_n \in \mathbb{R}^K, A \in \mathbb{R}^{N \times K}, A_{i,:} = (a_i)^T$) (Konno et al., 2021; Fujii et al., 2024). Here, K represents the highest atomic number considered. Since we are dealing with atomic numbers from 1 to 98, $K = 98$. When an element with the atomic number k occupies site n , a_n becomes a one-hot vector with the element k set to 1 and 0 at all others. Please refer to Section A.5 for a discussion on the general applicability of using atomic distributions in various property prediction models.

3.1 MASKS TO MAINTAIN ELECTRICAL NEUTRALITY

To maintain electrical neutrality, we restrict the possible values of atomic distribution \mathbf{a}_n by using a mask that aligns with the possible oxidation numbers at site n . These possible oxidation numbers are determined from the initial structure. Here, we explain this using the rutile type structure as an example. A typical material having this structure is titanium dioxide (TiO_2). The rutile TiO_2 contains one Ti site and two O sites, totaling three atomic sites. When titanium has an oxidation number of +4 and the two oxygen atoms each have an oxidation number of -2 , the total oxidation number is zero, thus achieving electrical neutrality. Therefore, to maintain electrical neutrality, we can use an atomic distribution that includes only elements with a +4 oxidation number, such as Ti and Mn at the Ti site. At the O sites, we use those with an oxidation number of -2 , such as O and S. This ensures electrical neutrality regardless of the elements selected after optimization. The adjusted atomic distribution \mathbf{a}'_n , which considers oxidation numbers, is obtained by taking the element-wise product of the learnable distribution \mathbf{a}_n with the atomic mask $\mathbf{m}(s)$.

$$\mathbf{a}'_n(s) = \sigma(\mathbf{m}(s) * \mathbf{a}_n) \quad (3)$$

Here, $\mathbf{m}(s)$ is $\mathbf{m}(s) \in \mathbb{R}^K$ and a mask that assigns a value of 1 to elements with the oxidation number s , and 0 to all others (Fig. 2(a)). σ is a normalization function that rescales all elements to the range $[0,1]$, with their total sum normalized to 1.0. The asterisk denotes element-wise multiplication. This process is applied to all sites, yielding an atomic distribution $\mathbf{A}'(\mathbf{S})$ that reflects the oxidation numbers for all sites.

$$\mathbf{A}'(\mathbf{S}) = \sigma_{\text{atom}}(\mathbf{A} * \mathbf{M}(\mathbf{S})) \quad (4)$$

$$\mathbf{M} \in \mathbb{R}^{N \times K}, \mathbf{M}(\mathbf{S})_{i,:} = (\mathbf{m}(s_i))^\top, \mathbf{S}_i = s_i, \mathbf{m}(s_i) \in \{\mathbf{m}(s_{\min}), \dots, \mathbf{m}(s), \dots, \mathbf{m}(s_{\max})\} \quad (5)$$

Here, σ_{atom} is a function that normalizes values along elemental directions. s_i is the oxidation number at site- i . The s_{\min} and s_{\max} respectively denote the minimum and maximum oxidation numbers among all elements considered. To simultaneously consider different patterns of oxidation number combinations, we introduce a learnable parameter \mathbf{o} , which selects the optimal combination of oxidation numbers. We illustrate this approach using CoF_2 and TiO_2 , both of which adopt the rutile structure. The oxidation numbers differ at each atomic site, with CoF_2 exhibiting oxidation numbers of $[+2, -1, -1]$ and TiO_2 having $[+4, -2, -2]$. The \mathbf{o} is a d -dimensional vector selecting the best pattern from d patterns of oxidation number combinations. The \mathbf{o} represents the probabilities of each combination. For instance, when considering two patterns, such as those of CoF_2 and TiO_2 , d equals 2. Using this framework, we can calculate the modified atomic distribution \mathbf{a}'_n (Fig. 2(b)) considering multiple combination patterns as follows:

$$\mathbf{a}'_n(\mathbf{a}_n, \mathbf{o}_d) = \sum_{d=1}^D \mathbf{a}'_{n,d} = \sum_{d=1}^D \sigma(\mathbf{m}(s_{n,d}) * \mathbf{a}_n) \mathbf{o}_d. \quad (6)$$

Here, $\mathbf{m}(s_{i,d}) \in \{\mathbf{m}(s_{\min}), \dots, \mathbf{m}(s), \dots, \mathbf{m}(s_{\max})\}$. The property prediction models assume that each site contains a single element. Therefore, after optimization, it is desirable for the oxidation state configuration parameter \mathbf{o} and atomic distributions \mathbf{a}'_n to become one-hot vectors. To guarantee that optimization will result in them becoming one-hot vectors, we normalize \mathbf{a}'_n and \mathbf{o} with the temperature softmax function σ_T .

$$\sigma_T(z_i) = \frac{\exp\left(\frac{z_i}{T}\right)}{\sum_j \exp\left(\frac{z_j}{T}\right)} \quad (7)$$

$$\tilde{\mathbf{o}} = \sigma_T(\mathbf{o}) \quad (8)$$

$$\tilde{\mathbf{A}}_n(\mathbf{A}_n, \mathbf{o}, T) = \sigma_T\left(\sum_{d=1}^D \mathbf{A}'_d(\mathbf{S}_d)\right) = \sigma_{T,\text{atom}}\left(\sum_{d=1}^D \sigma_{T,\text{atom}}(\mathbf{M}(\mathbf{S}_d) * \mathbf{A}) \tilde{\mathbf{o}}_d\right) \quad (9)$$

$$(\mathbf{M}(\mathbf{S}_d) \in \mathbb{R}^{N \times K}, \mathbf{M}(\mathbf{S}_d)_{i,:} = \mathbf{m}(s_{i,d})^\top, (\mathbf{S}_d)_i = s_{i,d} \quad (10)$$

Here, $M(S_d)$ is an atomic mask of the d -th oxidation pattern. σ_T produces sharper distributions at lower temperatures T , ensuring that the parameters transition into one-hot vectors. For example, let o_1 represent the probability of the TiO_2 type with oxidation numbers $[+4, -2, -2]$, and o_2 represent the CoF_2 type with oxidation numbers $[+2, -1, -1]$. If, at the end of optimization, $\mathbf{o} = (1., 0.)$ is achieved, the TiO_2 type is selected, resulting in a material with an oxidation pattern of $[+4, -2, -2]$, as shown in Fig. 2(c).

3.2 INITIALIZATION AND MULTIPLE PROPERTIES OPTIMIZATION

In SMOACS, the initial structures for the optimization process are obtained from two sources: an existing dataset and self-generated structures based on typical perovskites with modified lattice constants (for details, see Section A.6 and A.7). These crystal structures must satisfy electrical neutrality and generate D oxidation number patterns based on the compositions of initial crystal structures (see Section A.11 for details). The lattice constant l and atomic coordinates \mathbf{C} are used directly as initial values. The atomic distribution \mathbf{A} and the oxidation number pattern selection parameter \mathbf{o} are initialized with a uniform distribution.

$$\theta'_{\text{crystal}} = \tau\left(\{l, \mathbf{C}, \tilde{\mathbf{A}}(\mathbf{A}, \mathbf{o}, T), \tilde{\mathbf{o}}(\mathbf{o}, T)\}\right) \quad (11)$$

$$l \leftarrow -\eta_l \frac{\partial L}{\partial l}, \quad \mathbf{C} \leftarrow -\eta_C \frac{\partial L}{\partial \mathbf{C}}, \quad \mathbf{A} \leftarrow -\eta_A \frac{\partial L}{\partial \mathbf{A}}, \quad \mathbf{o} \leftarrow -\eta_o \frac{\partial L}{\partial \mathbf{o}}. \quad (12)$$

Here, $\eta_l, \eta_C, \eta_A, \eta_o$ denote the learning rates for each parameter. L denotes loss function $L(f_*(\theta'_{\text{crystal}}), \mathbf{y}_{\text{target}})$ and f_* denotes a set of trained models. The τ is a function converting structures to inputs for f_* . We optimize structures by iteratively updating them using Eq. 11 and 12. During optimization, the temperature T of the softmax function starts high and is lowered towards the end, forcing $\tilde{\mathbf{o}}$ and $\tilde{\mathbf{a}}_n$ into one-hot vectors in the final stage. SMOACS optimizes multiple properties by incorporating various trained models or additional loss functions. Here, we aim to optimize the crystal structure by minimizing formation energy and targeting a specific band gap range, $y_{\text{bg}} \pm h_{\text{bg}}$, using trained models $f_* = \{f_{\text{bg}*}, f_{\text{f}*}\}$. Here, h_{bg} is an acceptable margin and $f_{\text{bg}*}$ is the trained model predicting the band gap, and $f_{\text{f}*}$ predicts the formation energy. We also set a strength parameter λ .

$$L_{\text{bg}}(y_{\text{bg}}, \hat{y}_{\text{bg}}) = \max(0, |y_{\text{bg}} - \hat{y}_{\text{bg}}| - h_{\text{bg}}), \quad L_{\text{f}}(\hat{y}_{\text{f}}) = \hat{y}_{\text{f}} \quad (13)$$

$$L = L_{\text{bg}}(y_{\text{bg}}, f_{\text{bg}*}(\theta'_{\text{crystal}})) + \lambda L_{\text{f}}(f_{\text{f}*}(\theta'_{\text{crystal}})) \quad (14)$$

The influence of λ is discussed in Section A.12. Note that since the crystal structure changes during optimization, when using GNNs, we update the graph multiple times based on the current structure in the optimization process.

3.3 PRESERVATION OF SPECIFIC CRYSTAL STRUCTURES DURING OPTIMIZATION

Limiting the optimization variables and their range allows us to maintain specific crystal structures during optimization. For instance, let us consider a typical perovskite structure, represented by the chemical formula ABX_3 . It consists of five sites and adopts a crystal structure close to a cubic lattice. The fractional coordinates for the five sites are as follows: $(0.5, 0.5, 0.5)$ at the A site, $(0.0, 0.0, 0.0)$ at the B site, and $(0.5, 0.0, 0.0)$, $(0.0, 0.5, 0.0)$, $(0.0, 0.0, 0.5)$ at the three X sites. Note that deviations from these values are allowed, together with degrees of freedom related to the lattice constant values. We optimize the structures within the range of small perturbations applied to typical perovskites. Specifically, first, only the a, b , and c of l are optimized, while α, β , and γ are fixed at 90° . Subsequently, the optimization range for the five sites is set close to their typical coordinates. For example, we optimize the coordinates at the A site within the range $(0.5 \pm \epsilon, 0.5 \pm \epsilon, 0.5 \pm \epsilon)$, where ϵ is a small constant. Following a previous work on the distortion of $\text{CaCu}_3\text{Ti}_4\text{O}_{12}$ (Božin et al., 2004), we set $\epsilon = 0.15$. We also specify possible patterns of oxidation number combinations. Typically, some materials with perovskite structure such as SrTiO_3 exhibit oxidation numbers of $[+2, +4, -2]$ at the A, B, and X sites, respectively, while others such as $(\text{CH}_3\text{NH}_3)\text{PbI}_3$ exhibit $[+1, +2, -1]$. Consequently, two oxidation number patterns are prepared for the perovskite structure: $[+2, +4, -2]$ and $[+1, +2, -1]$ for the A, B, and X sites, respectively. By specifying these variables and ranges for optimization, we are able to maintain the perovskite structure.

4 EXPERIMENTS

We compare SMOACS’s ability to propose material satisfying specified properties and constraints with those from deep generative models and Bayesian optimization, represented by FTCP and TPE, respectively. TPE was chosen over GP, as discussed in Section 2. Both SMOACS and TPE ran for 200 optimization steps. All models were trained on the MEGNet dataset. For further implementation details, please refer to Section A.4. To demonstrate SMOACS’s versatility across various property prediction models, we conducted optimizations using ALIGNN and Crystalformer, GNN-based and transformer-based models, respectively. We evaluated the optimized materials using three metrics: whether they satisfied the specified criteria on the band gap range, formation energy, and validity of crystal structure. Specifically, we judge that the formation energy criterion is satisfied if it is less than -0.5 eV, and for the validity of crystal structure, following a previous research (Xie et al., 2022), we adopted two criteria: all interatomic distances being at least 0.5 Å and maintaining electrical neutrality. For assessing electrical neutrality, we consider the material electrically neutral if the sum of possible oxidation numbers for atoms at each site equals zero. Please refer to Section A.9 for details. For experiments utilizing models trained on datasets other than MEGNet, please refer to Section A.13.

4.1 LEVERAGING THE LATEST RESEARCH ACHIEVEMENTS IN PROPERTY PREDICTION

First, we experimented with the performance of property prediction models that could be adopted in systems such as SMOACS, Bayesian optimization (TPE), or FTCP. In principle, Bayesian optimization—a type of black-box optimization—and SMOACS can adopt a broad range of property prediction models. Meanwhile, FTCP—a generative model—employs a property prediction branch within its architecture. Therefore, unlike SMOACS and Bayesian optimization, FTCP cannot use ALIGNN or Crystalformer for property predictions. The results are shown in Table 1.

Crystalformer demonstrated the highest prediction accuracy among the models in Table 1. ALIGNN ranked second, whereas the prediction branches of FTCP exhibited the lowest performance. This result confirmed an advantage of SMOACS and TPE: their ability to incorporate state-of-the-art property prediction models, such as Crystalformer and ALIGNN, allowing for highly accurate material property predictions.

4.2 SIMULTANEOUS OPTIMIZATION OF TARGETED PROPERTIES REGARDLESS OF THE CRYSTAL STRUCTURE

We tested the ability to optimize band gaps to target values. In this experiment, we optimized both the band gap and formation energy simultaneously, regardless of the crystal structure. To ensure a fair comparison of optimization methods, we fixed the margin for all band gaps at ± 0.04 eV. For optimization results where the predictor’s error is used as the margin, please refer to Section A.14. We conducted experiments with SMOACS using Crystalformer and ALIGNN, respectively. We utilized Crystalformer as a predictor for TPE. We used three objective functions for TPE: band gap, formation energy, and electrical neutrality. FTCP selected data from the MEGNet dataset close to the target band gap and with formation energy less than -0.5 eV, subsequently encoding them into latent variables. Finally, after adding noise, we decoded them back into crystal structures for evaluation. We optimized and evaluated the structures based on the band gap and formation energy values predicted by their respective predictors.

Table 1: Comparison of property prediction models. This table compares models trained on the MEGNet dataset and presents Mean Absolute Error (MAE) scores for formation energy (**E_{form}**) and band gap on test data in the MEGNet dataset. Lower scores are better across all metrics.

Prediction Model	Applicable Method	E _{form} MAE (eV)	Band Gap MAE (eV)
Prediction Branch of FTCP	FTCP	0.224	0.442
ALIGNN	SMOACS, TPE	0.022	0.218
Crystalformer	SMOACS, TPE	0.019	0.198

Table 2: Experiments on optimizing band gaps. We define the success rate as the probability of simultaneously satisfying three conditions: (A) the band gap is optimized within the target range, (B) the formation energy is below -0.5 eV, and (C) the crystal structure is valid. C is achieved when two criteria are met simultaneously: (a) all inter-atomic distances are greater than 0.5 Å, and (b) the structure is electrically neutral. S(Cry) and S(ALI) denote SMOACS utilizing the Crystalformer and ALIGNN models, respectively. We evaluated each of the proposed materials using all evaluation metrics, and the results were averaged over 256 samples. Higher scores are better across all metrics. Augmented results are shown in Table A.2.

Target BG (eV)	method	success rate	(A)BG	(B) E_f	(C)STR	(a) neut	(b) 0.5Å
0.50 ± 0.04	S(Cry)	0.328	0.465	0.566	0.758	0.957	0.758
	S(ALI)	0.055	0.062	0.867	0.867	0.949	0.867
	TPE	0.004	0.945	0.059	0.066	0.070	0.910
	FTCP	0.000	0.004	1.000	0.719	0.746	0.906
1.50 ± 0.04	S(Cry)	0.387	0.543	0.672	0.824	0.980	0.824
	S(ALI)	0.043	0.066	0.828	0.852	0.938	0.852
	TPE	0.020	0.855	0.055	0.074	0.082	0.828
	FTCP	0.000	0.000	1.000	0.703	0.723	0.895
2.50 ± 0.04	S(Cry)	0.383	0.473	0.715	0.840	0.984	0.840
	S(ALI)	0.051	0.059	0.809	0.793	0.898	0.793
	TPE	0.023	0.711	0.098	0.051	0.055	0.816
	FTCP	0.004	0.004	1.000	0.695	0.707	0.902

The results are shown in Table 2. SMOACS significantly outperformed both TPE and FTCP in terms of success rates. SMOACS consistently maintained electrical neutrality, except for extreme geometries causing NaN values during crystal vector calculations. While FTCP always met the requirements for formation energy, it struggled to achieve the target band gap, contributing to its lower overall success rate. TPE achieved a high success rate in optimizing the band gap within the target range, but it could not optimize formation energy well. SMOACS maintained a high overall success rate as it achieved substantial success rates in both band gap and formation energy optimization. SMOACS can easily scale this computation and can optimize 2,048 samples simultaneously in just a few minutes using a single A100 GPU. This allows us to repeat the optimization process multiple times, enabling us to obtain a large number of successful optimization samples. Please refer to Section A.6 for details, including the diversity of generated materials.

4.3 SIMULTANEOUS OPTIMIZATION OF TARGETED PROPERTIES WHILE PRESERVING PEROVSKITE STRUCTURES

We optimized the band gap within the range of 0.5 to 2.5 eV while preserving the perovskite structure. Besides the previously discussed metrics, we used three new criteria to confirm a structure’s perovskite identity: internal coordinates, angles between crystal axes, and the tolerance factor. The tolerance factor t serves as a metric to assess the suitability of atomic combinations for forming perovskite structures (West, 2022). t is calculated based on the ionic radii r_A , r_B and r_X of each site in the perovskite structure ABX_3 and we employed a loss function to optimize the tolerance factor alongside minimizing the band gap and formation energy.

$$t = \frac{r_A + r_X}{\sqrt{2}(r_B + r_X)} \quad (15)$$

$$L_t = |t - 0.9| \quad (16)$$

$$L = L_{bg}(y_{bg}, f_{bg*}(\theta'_{crystal})) + L_f(f_{f*}(\theta'_{crystal})) + L_t(\theta'_{crystal}) \quad (17)$$

If t is close to 1, the structure is likely a perovskite; if it is far from 1, it is not. Considering t values of typical perovskite structures (BaCeO₃:0.857, SrTiO₃: 0.910 and BaTiO₃: 0.970), we established a tolerance factor range of $0.8 \leq t \leq 1.0$ as the criterion for success. SMOACS optimized the structures with the procedure outlined in Section 3.3. Due to the limited number of perovskite

Table 3: Experiments on optimizing various band gaps while preserving perovskite structures. The "success rate" is the probability of simultaneously satisfying four criteria: (A) the band gap is optimized within the target range, (B) the formation energy is below -0.5 eV, (C) the crystal structure is valid, and (D) approximating a valid perovskite structure. Criteria (A), (B), and (C) are consistent with those outlined in Table 2. The (D) is achieved when three criteria are met simultaneously: (c) the tolerance factor t is between 0.8 and 1.0, (d) coordinates are within ± 0.15 of typical perovskite structure coordinates, and (e) crystal axis angles are from 85° to 95° . The results are averaged over 256 samples. Higher scores are better across all metrics. Augmented results are shown in Table A.4.

Target BG (eV)	method	success rate	(A)BG	(B) E_f	(C)STR	(a) neut	(b) 0.5\AA	(D)PS	(c) tole	(d) angles	(e) coord
0.50 ± 0.04	S(Cry)	0.113	0.477	0.410	0.965	1.000	0.965	0.500	0.500	1.000	1.000
	S(ALI)	0.090	0.211	0.535	1.000	1.000	1.000	0.500	0.500	1.000	1.000
	TPE	0.027	1.000	0.137	0.535	0.535	1.000	0.648	0.648	1.000	1.000
	FTCP	0.004	0.023	1.000	0.836	0.840	0.938	0.258	0.508	0.441	0.285
1.50 ± 0.04	S(Cry)	0.148	0.422	0.461	0.984	1.000	0.984	0.578	0.578	1.000	1.000
	S(ALI)	0.070	0.219	0.652	1.000	1.000	1.000	0.629	0.629	1.000	1.000
	TPE	0.023	0.992	0.281	0.293	0.293	1.000	0.523	0.523	1.000	1.000
	FTCP	0.000	0.016	1.000	0.895	0.906	0.965	0.242	0.547	0.418	0.320
2.50 ± 0.04	S(Cry)	0.152	0.285	0.516	0.988	1.000	0.988	0.625	0.625	1.000	1.000
	S(ALI)	0.113	0.184	0.938	1.000	1.000	1.000	0.625	0.625	1.000	1.000
	TPE	0.016	0.918	0.281	0.352	0.352	1.000	0.387	0.387	1.000	1.000
	FTCP	0.008	0.012	0.996	0.879	0.898	0.953	0.250	0.543	0.441	0.289

structures in the MEGNet dataset, random perovskite configurations are used as initial values for SMOACS and TPE. The optimization range for SMOACS and TPE is established as outlined in Section 3.3. FTCP initially encoded typical perovskite structures from the MEGNet dataset into latent variables. After adding noise, these latent variables are decoded back into crystal structures for evaluation. Please refer to Section A.7 for details, including the diversity analysis. We evaluated the structures based on the band gap and formation energy values predicted by their respective predictors. The evaluation results are shown in Table 3.

SMOACS with Crystalformer significantly outperformed both TPE and FTCP in overall success rates while preserving perovskite structures. In terms of (d) coordinates and (e) angles, both SMOACS and TPE consistently meet the criteria because their optimization ranges are the same. The generative model (FTCP), which uses latent variables, fails to obtain specific structural features of perovskite. Note that this limitation occurs despite the use of latent variables based on typical perovskite structures. This seems to be attributed to the training dataset that includes mixed crystal types. It is noteworthy that SMOACS consistently ensures electrical neutrality.

4.4 OPTIMIZING LARGE ATOMIC CONFIGURATIONS

We optimized large atomic configurations where calculating electrical neutrality is impractical. In systems containing many atoms, the calculation of electrical neutrality becomes infeasible due to combinatorial explosion. For example, a system containing 135 atoms, each with two possible oxidation numbers, results in about 4.3×10^{40} combinations. Therefore, including an objective function for electrical neutrality in the TPE is infeasible. We conducted experiments on $3 \times 3 \times 3$ perovskite structures containing 135 atom sites and compared SMOACS with TPE, not including the objective function for electrical neutrality (referred to as TPE(N)). The results are shown in Table 4.

SMOACS successfully optimized large atomic configurations, while TPE(N) failed due to its inability to optimize the formation energy. The success of SMOACS likely stems from the utilization of information on gradients to optimize based on physics, enabling optimization even in large and complex systems. Furthermore, TPE was not able to evaluate electrical neutrality due to the computational cost of calculating it. Conversely, since SMOACS always maintains electrical neutrality, it is able to optimize properties while preserving this neutrality. Please refer to Section A.8 for details.

Table 4: Experiments optimizing for various band gaps while preserving $3 \times 3 \times 3$ perovskite structures. We include only TPE, showing better performance in Section 4.3, for comparison. Evaluation methods are based on those described in Table 3. Augmented results are shown in Table A.6.

Target BG (eV)	method	success rate	(A)BG	(B) E_f	(C)STR	(a) neut	(b) 0.5Å	(D)PS	(c) tole	(d) angles	(e) coord
0.50 ± 0.04	S(Cry)	0.156	0.734	0.547	0.968	1.00	0.969	0.570	0.570	1.000	1.000
	S(ALI)	0.188	0.234	0.812	0.687	1.00	0.688	0.789	0.789	1.000	1.000
	TPE(/N)	0.000	1.000	0.000	-	N/A	1.000	0.609	0.609	1.000	1.000
1.50 ± 0.04	S(Cry)	0.047	0.125	0.422	0.953	1.00	0.953	0.617	0.617	1.000	1.000
	S(ALI)	0.062	0.086	0.867	0.726	1.00	0.727	0.586	0.586	1.000	1.000
	TPE(/N)	0.000	0.141	0.000	-	N/A	1.000	0.180	0.180	1.000	1.000
2.50 ± 0.04	S(Cry)	0.023	0.039	0.438	0.984	1.00	0.984	0.664	0.664	1.000	1.000
	S(ALI)	0.102	0.172	1.000	0.703	1.00	0.703	0.812	0.812	1.000	1.000
	TPE(/N)	0.000	0.023	0.000	-	N/A	0.984	0.156	0.156	1.000	1.000

4.5 VERIFICATION BY DENSITY FUNCTIONAL THEORY

We used Density Functional Theory (see Section A.1 for details) to verify the band gaps of materials proposed by SMOACS. Among these materials, BaCsFCII (Fig. 1(right)), a perovskite structured for a 4.02 eV band gap, showed a DFT-calculated value of 3.96 eV. However, we also found discrepancies between the values the model predicted and the DFT calculated for other candidate materials. Detailed results can be found in the appendix, Section A.2.

5 CONCLUSIONS

We propose SMOACS, a framework that utilizes the latest high-accuracy property prediction models and their gradients to search for materials with targeted multiple properties. SMOACS can adaptively apply constraints such as electrical neutrality and specific crystal structures without re-training. SMOACS not only outperformed FTCP and TPE in optimizing multiple targeted properties simultaneously but also maintained electrical neutrality in large systems where calculating electrical neutrality is challenging due to combinatorial complexity. As a further potential application, SMOACS should facilitate the exploration of stable structures. Using a compositional formula and various structure candidates they could form, this method minimizes formation energy while maintaining the crystal structure, thus determining the most stable configuration for that formula (see Section A.3). However, the performance of SMOACS heavily depends on the accuracy of property prediction models. Using models based on DFT calculations that underestimate band gaps (see Section A.2) can lead to similar underestimations in the predictions. By adopting more accurate models trained on datasets that are large and developed with more accurate DFT, we may address these challenges.

REFERENCES

- Mila AI4Science, Alex Hernandez-Garcia, Alexandre Duval, Alexandra Volokhova, Yoshua Bengio, Divya Sharma, Pierre Luc Carrier, Yasmine Benabed, Michał Koziarski, and Victor Schmidt. Crystal-gfn: sampling crystals with desirable properties and constraints. *arXiv preprint arXiv:2310.04925*, 2023.
- Takuya Akiba, Shotaro Sano, Toshihiko Yanase, Takeru Ohta, and Masanori Koyama. Optuna: A next-generation hyperparameter optimization framework. In *Proceedings of the 25th ACM SIGKDD International Conference on Knowledge Discovery & Data Mining*, KDD '19, pp. 2623–2631, New York, NY, USA, 2019. Association for Computing Machinery. ISBN 9781450362016. doi: 10.1145/3292500.3330701. URL <https://doi.org/10.1145/3292500.3330701>.
- Kelsey R Allen, Tatiana Lopez-Guevara, Kimberly Stachenfeld, Alvaro Sanchez-Gonzalez, Peter Battaglia, Jessica Hamrick, and Tobias Pfaff. Physical design using differentiable learned simulators. *arXiv preprint arXiv:2202.00728*, 2022.

- 540 P. E. Blöchl. Projector augmented-wave method. *Phys. Rev. B*, 50:17953–17979, Dec 1994. doi: 10.
541 1103/PhysRevB.50.17953. URL [https://link.aps.org/doi/10.1103/PhysRevB.](https://link.aps.org/doi/10.1103/PhysRevB.50.17953)
542 50.17953.
- 543 Giovanni Bordiga, Eder Medina, Sina Jafarzadeh, Cyrill Bösch, Ryan P Adams, Vincent Tournat,
544 and Katia Bertoldi. Automated discovery of reprogrammable nonlinear dynamic metamaterials.
545 *Nature Materials*, pp. 1–9, 2024.
- 546 Onur Boyar, Yanheng Gu, Yuji Tanaka, Shunsuke Tonogai, Tomoya Itakura, and Ichiro Takeuchi.
547 Crystal-Isbo: Automated design of de novo crystals with latent space bayesian optimization. *arXiv*
548 *preprint arXiv:2405.17881*, 2024.
- 549 E S Božin, V Petkov, P W Barnes, P M Woodward, T Vogt, S D Mahanti, and S J L Billinge.
550 Temperature dependent total scattering structural study of cacu3ti4o12. *Journal of Physics: Con-*
551 *densed Matter*, 16(44):S5091, oct 2004. doi: 10.1088/0953-8984/16/44/007. URL [https:](https://dx.doi.org/10.1088/0953-8984/16/44/007)
552 [//dx.doi.org/10.1088/0953-8984/16/44/007](https://dx.doi.org/10.1088/0953-8984/16/44/007).
- 553 Tom Brown, Benjamin Mann, Nick Ryder, Melanie Subbiah, Jared D Kaplan, Prafulla Dhari-
554 wal, Arvind Neelakantan, Pranav Shyam, Girish Sastry, Amanda Askell, Sandhini Agar-
555 wal, Ariel Herbert-Voss, Gretchen Krueger, Tom Henighan, Rewon Child, Aditya Ramesh,
556 Daniel Ziegler, Jeffrey Wu, Clemens Winter, Chris Hesse, Mark Chen, Eric Sigler, Mateusz
557 Litwin, Scott Gray, Benjamin Chess, Jack Clark, Christopher Berner, Sam McCandlish, Alec
558 Radford, Ilya Sutskever, and Dario Amodei. Language models are few-shot learners. In
559 H. Larochelle, M. Ranzato, R. Hadsell, M.F. Balcan, and H. Lin (eds.), *Advances in Neu-*
560 *ral Information Processing Systems*, volume 33, pp. 1877–1901. Curran Associates, Inc.,
561 2020. URL [https://proceedings.neurips.cc/paper_files/paper/2020/](https://proceedings.neurips.cc/paper_files/paper/2020/file/1457c0d6bfcb4967418bf8ac142f64a-Paper.pdf)
562 [file/1457c0d6bfcb4967418bf8ac142f64a-Paper.pdf](https://proceedings.neurips.cc/paper_files/paper/2020/file/1457c0d6bfcb4967418bf8ac142f64a-Paper.pdf).
- 563 Chi Chen, Weike Ye, Yunxing Zuo, Chen Zheng, and Shyue Ping Ong. Graph networks as a universal
564 machine learning framework for molecules and crystals. *Chemistry of Materials*, 31(9):3564–
565 3572, 2019.
- 566 Hitarth Choubisa, Petar Todorović, Joao M Pina, Darshan H Parmar, Ziliang Li, Oleksandr Voznyy,
567 Isaac Tamblyn, and Edward H Sargent. Interpretable discovery of semiconductors with machine
568 learning. *npj Computational Materials*, 9(1):117, 2023.
- 569 Kamal Choudhary. Alignn models on jarvis-dft dataset, 2021. URL 10.6084/m9.figshare.
570 17005681.v6.
- 571 Kamal Choudhary and Brian DeCost. Atomistic line graph neural network for improved materials
572 property predictions. *npj Computational Materials*, 7(1):185, 2021.
- 573 Ali Davariashtiyani and Sara Kadkhodaei. Formation energy prediction of crystalline compounds
574 using deep convolutional network learning on voxel image representation. *Communications Ma-*
575 *terials*, 4(1):105, 2023.
- 576 Daniel W. Davies, Keith T. Butler, Adam J. Jackson, Jonathan M. Skelton, Kazuki Morita, and
577 Aron Walsh. Smact: Semiconducting materials by analogy and chemical theory. *Journal of Open*
578 *Source Software*, 4(38):1361, 2019. doi: 10.21105/joss.01361. URL [https://doi.org/10.](https://doi.org/10.21105/joss.01361)
579 [21105/joss.01361](https://doi.org/10.21105/joss.01361).
- 580 Qianggang Ding, Santiago Miret, and Bang Liu. Matexpert: Decomposing materials discovery by
581 mimicking human experts. *arXiv preprint arXiv:2410.21317*, 2024.
- 582 Alexey Dosovitskiy, Lucas Beyer, Alexander Kolesnikov, Dirk Weissenborn, Xiaohua Zhai, Thomas
583 Unterthiner, Mostafa Dehghani, Matthias Minderer, Georg Heigold, Sylvain Gelly, Jakob Uszko-
584 reit, and Neil Houlsby. An image is worth 16x16 words: Transformers for image recogni-
585 tion at scale. In *International Conference on Learning Representations*, 2021. URL [https:](https://openreview.net/forum?id=YicbFdNTTy)
586 [//openreview.net/forum?id=YicbFdNTTy](https://openreview.net/forum?id=YicbFdNTTy).
- 587 Akihiro Fujii, Hideki Tsunashima, Yoshihiro Fukuhara, Koji Shimizu, and Satoshi Watanabe. En-
588 hancing inverse problem solutions with accurate surrogate simulators and promising candidates.
589 *arXiv preprint arXiv:2304.13860*, 2023.

- 594 Akihiro Fujii, Koji Shimizu, and Satoshi Watanabe. Efficient exploration of high-*tc* superconductors
595 by a gradient-based composition design. *arXiv preprint arXiv:2403.13627*, 2024.
596
- 597 Prashant Govindarajan, Santiago Miret, Jarrid Rector-Brooks, Mariano Phielipp, Janarthanan Ra-
598 jendran, and Sarath Chandar. Learning conditional policies for crystal design using offline rein-
599 forcement learning. *Digital Discovery*, 3(4):769–785, 2024.
- 600 Martin A Green, Anita Ho-Baillie, and Henry J Snaith. The emergence of perovskite solar cells.
601 *Nature photonics*, 8(7):506–514, 2014.
602
- 603 Nate Gruver, Anuroop Sriram, Andrea Madotto, Andrew Gordon Wilson, C Lawrence Zitnick, and
604 Zachary Ulissi. Fine-tuned language models generate stable inorganic materials as text. *arXiv*
605 *preprint arXiv:2402.04379*, 2024.
606
- 607 Jonathan Ho and Tim Salimans. Classifier-free diffusion guidance. In *NeurIPS 2021 Workshop on*
608 *Deep Generative Models and Downstream Applications*, 2021. URL <https://openreview.net/forum?id=qw8AKxfYbI>.
609
- 610 Rakhoon Hwang, Jae Yong Lee, Jin Young Shin, and Hyung Ju Hwang. Solving pde-constrained
611 control problems using operator learning. In *Proceedings of the AAAI Conference on Artificial*
612 *Intelligence*, volume 36, pp. 4504–4512, 2022.
613
- 614 Anubhav Jain, Shyue Ping Ong, Geoffroy Hautier, Wei Chen, William Davidson Richards, Stephen
615 Dacek, Shreyas Cholia, Dan Gunter, David Skinner, Gerbrand Ceder, and Kristin A. Persson.
616 Commentary: The Materials Project: A materials genome approach to accelerating materials
617 innovation. *APL Materials*, 1(1):011002, 07 2013. ISSN 2166-532X. doi: 10.1063/1.4812323.
618 URL <https://doi.org/10.1063/1.4812323>.
- 619 Rui Jiao, Wenbing Huang, Peijia Lin, Jiaqi Han, Pin Chen, Yutong Lu, and Yang Liu. Crystal
620 structure prediction by joint equivariant diffusion. *Advances in Neural Information Processing*
621 *Systems*, 36, 2024.
622
- 623 Danial Khatamsaz, Raymond Neuberger, Arunabha M Roy, Sina Hossein Zadeh, Richard Otis, and
624 Raymundo Arróyave. A physics informed bayesian optimization approach for material design:
625 application to niti shape memory alloys. *npj Computational Materials*, 9(1):221, 2023.
- 626 Diederik P Kingma. Auto-encoding variational bayes. *arXiv preprint arXiv:1312.6114*, 2013.
627
- 628 Tomohiko Konno, Hodaka Kurokawa, Fuyuki Nabeshima, Yuki Sakishita, Ryo Ogawa, Iwao
629 Hosako, and Atsutaka Maeda. Deep learning model for finding new superconductors. *Phys.*
630 *Rev. B*, 103:014509, Jan 2021. doi: 10.1103/PhysRevB.103.014509. URL <https://link.aps.org/doi/10.1103/PhysRevB.103.014509>.
631
- 632 G. Kresse and D. Joubert. From ultrasoft pseudopotentials to the projector augmented-wave method.
633 *Phys. Rev. B*, 59:1758–1775, Jan 1999. doi: 10.1103/PhysRevB.59.1758. URL <https://link.aps.org/doi/10.1103/PhysRevB.59.1758>.
634
635
- 636 Aliaksandr V Kruckau, Oleg A Vydrov, Artur F Izmaylov, and Gustavo E Scuseria. Influence of the
637 exchange screening parameter on the performance of screened hybrid functionals. *The Journal of*
638 *chemical physics*, 125(22), 2006.
639
- 640 Yuchao Lin, Keqiang Yan, Youzhi Luo, Yi Liu, Xiaoning Qian, and Shuiwang Ji. Efficient approxi-
641 mations of complete interatomic potentials for crystal property prediction. In Andreas Krause,
642 Emma Brunskill, Kyunghyun Cho, Barbara Engelhardt, Sivan Sabato, and Jonathan Scarlett
643 (eds.), *Proceedings of the 40th International Conference on Machine Learning*, volume 202 of
644 *Proceedings of Machine Learning Research*, pp. 21260–21287. PMLR, 23–29 Jul 2023. URL
645 <https://proceedings.mlr.press/v202/lin23m.html>.
- 646 Steph-Yves Louis, Yong Zhao, Alireza Nasiri, Xiran Wang, Yuqi Song, Fei Liu, and Jianjun Hu.
647 Graph convolutional neural networks with global attention for improved materials property pre-
prediction. *Physical Chemistry Chemical Physics*, 22(32):18141–18148, 2020.

- 648 Tian Lu, Hongyu Li, Minjie Li, Shenghao Wang, and Wencong Lu. Inverse design of hybrid organic–
649 inorganic perovskites with suitable bandgaps via proactive searching progress. *ACS omega*, 7(25):
650 21583–21594, 2022.
- 651 Peder Lyngby and Kristian Sommer Thygesen. Data-driven discovery of 2d materials by deep
652 generative models. *npj Computational Materials*, 8(1):232, 2022.
- 653 Amil Merchant, Simon Batzner, Samuel S Schoenholz, Muratahan Aykol, Gowoon Cheon, and
654 Ekin Dogus Cubuk. Scaling deep learning for materials discovery. *Nature*, 624(7990):80–85,
655 2023.
- 656 Benjamin Kurt Miller, Ricky TQ Chen, Anuroop Sriram, and Brandon M Wood. Flowmm: Gener-
657 ating materials with riemannian flow matching. *arXiv preprint arXiv:2406.04713*, 2024.
- 658 Koichi Momma and Fujio Izumi. VESTA3 for three-dimensional visualization of crystal, volumetric
659 and morphology data. *Journal of Applied Crystallography*, 44(6):1272–1276, Dec 2011. doi: 10.
660 1107/S0021889811038970. URL <https://doi.org/10.1107/S0021889811038970>.
- 661 Shyue Ping Ong, William Davidson Richards, Anubhav Jain, Geoffroy Hautier, Michael Kocher,
662 Shreyas Cholia, Dan Gunter, Vincent L. Chevrier, Kristin A. Persson, and Gerbrand Ceder.
663 Python materials genomics (pymatgen): A robust, open-source python library for materials anal-
664 ysis. *Computational Materials Science*, 68:314–319, 2013. ISSN 0927-0256. doi: <https://doi.org/10.1016/j.commatsci.2012.10.028>. URL <https://www.sciencedirect.com/science/article/pii/S0927025612006295>.
- 665 Yoshihiko Ozaki, Yuta Suzuki, Takafumi Hawaii, Kotaro Saito, Masaki Onishi, and Kanta Ono. Au-
666 tomated crystal structure analysis based on blackbox optimisation. *npj Computational Materials*,
667 6(1):1–7, 2020a.
- 668 Yoshihiko Ozaki, Yuki Tanigaki, Shuhei Watanabe, and Masaki Onishi. Multiobjective tree-
669 structured parzen estimator for computationally expensive optimization problems. In *Proceed-*
670 *ings of the 2020 Genetic and Evolutionary Computation Conference, GECCO '20*, pp. 533–541,
671 New York, NY, USA, 2020b. Association for Computing Machinery. ISBN 9781450371285. doi:
672 10.1145/3377930.3389817. URL <https://doi.org/10.1145/3377930.3389817>.
- 673 Yoshihiko Ozaki, Yuki Tanigaki, Shuhei Watanabe, Masahiro Nomura, and Masaki Onishi. Multi-
674 objective tree-structured parzen estimator. *Journal of Artificial Intelligence Research*, 73:1209–
675 1250, 2022.
- 676 Cheol Woo Park and Chris Wolverton. Developing an improved crystal graph convolutional neural
677 network framework for accelerated materials discovery. *Phys. Rev. Mater.*, 4:063801, Jun
678 2020. doi: 10.1103/PhysRevMaterials.4.063801. URL <https://link.aps.org/doi/10.1103/PhysRevMaterials.4.063801>.
- 679 Adam Paszke, Sam Gross, Francisco Massa, Adam Lerer, James Bradbury, Gregory Chanan, Trevor
680 Killeen, Zeming Lin, Natalia Gimelshein, Luca Antiga, Alban Desmaison, Andreas Kopf, Edward
681 Yang, Zachary DeVito, Martin Raison, Alykhan Tejani, Sasank Chilamkurthy, Benoit Steiner,
682 Lu Fang, Junjie Bai, and Soumith Chintala. Pytorch: An imperative style, high-performance
683 deep learning library. In H. Wallach, H. Larochelle, A. Beygelzimer, F. d'Alché-Buc, E. Fox,
684 and R. Garnett (eds.), *Advances in Neural Information Processing Systems*, volume 32. Cur-
685 ran Associates, Inc., 2019. URL [https://proceedings.neurips.cc/paper_files/
686 paper/2019/file/bdbca288fee7f92f2bfa9f7012727740-Paper.pdf](https://proceedings.neurips.cc/paper_files/paper/2019/file/bdbca288fee7f92f2bfa9f7012727740-Paper.pdf).
- 687 John P. Perdew, Kieron Burke, and Matthias Ernzerhof. Generalized gradient approximation made
688 simple. *Phys. Rev. Lett.*, 77:3865–3868, Oct 1996. doi: 10.1103/PhysRevLett.77.3865. URL
689 <https://link.aps.org/doi/10.1103/PhysRevLett.77.3865>.
- 690 Simiao Ren, Willie Padilla, and Jordan Malof. Benchmarking deep inverse models over time,
691 and the neural-adjoint method. In H. Larochelle, M. Ranzato, R. Hadsell, M.F. Balcan, and
692 H. Lin (eds.), *Advances in Neural Information Processing Systems*, volume 33, pp. 38–48. Cur-
693 ran Associates, Inc., 2020. URL [https://proceedings.neurips.cc/paper_files/
694 paper/2020/file/007ff380ee5ac49ffc34442f5c2a2b86-Paper.pdf](https://proceedings.neurips.cc/paper_files/paper/2020/file/007ff380ee5ac49ffc34442f5c2a2b86-Paper.pdf).

- 702 Zekun Ren, Siyu Isaac Parker Tian, Juhwan Noh, Felipe Oviedo, Guangzong Xing, Jiali Li, Qiao-
703 hao Liang, Ruiming Zhu, Armin G. Aberle, Shijing Sun, Xiaonan Wang, Yi Liu, Qianxiao Li,
704 Senthilnath Jayavelu, Kedar Hippalgaonkar, Yousung Jung, and Tonio Buonassisi. An invert-
705 ible crystallographic representation for general inverse design of inorganic crystals with targeted
706 properties. *Matter*, 5(1):314–335, 2022. ISSN 2590-2385.
- 707 Kevin Ryan, Jeff Lengyel, and Michael Shatruk. Crystal structure prediction via deep learning.
708 *Journal of the American Chemical Society*, 140(32):10158–10168, 2018.
- 709 Jonathan Schmidt, Love Pettersson, Claudio Verdozzi, Silvana Botti, and Miguel AL Marques.
710 Crystal graph attention networks for the prediction of stable materials. *Science advances*, 7(49):
711 eabi7948, 2021.
- 712 Zhilong Song, Linfeng Fan, Shuaihua Lu, Qionghua Zhou, Chongyi Ling, and Jinlan Wang. In-
713 verse design of promising alloys for electrocatalytic CO_2 reduction via generative graph neural
714 networks combined with bird swarm algorithm. *arXiv preprint arXiv:2405.18891*, 2024.
- 715 Arsen Sultanov, Jean-Claude Crivello, Tabea Rebafka, and Nataliya Sokolovska. Data-driven score-
716 based models for generating stable structures with adaptive crystal cells. *Journal of Chemical*
717 *Information and Modeling*, 63(22):6986–6997, 2023.
- 718 Tatsunori Taniai, Ryo Igarashi, Yuta Suzuki, Naoya Chiba, Kotaro Saito, Yoshitaka Ushiku, and
719 Kanta Ono. Crystalformer: Infinitely connected attention for periodic structure encoding. In *The*
720 *Twelfth International Conference on Learning Representations*, 2024.
- 721 Ashish Vaswani, Noam Shazeer, Niki Parmar, Jakob Uszkoreit, Llion Jones, Aidan N Gomez,
722 Łukasz Kaiser, and Illia Polosukhin. Attention is all you need. In *Advances in Neural Infor-*
723 *mation Processing Systems*, volume 30. Curran Associates, Inc., 2017.
- 724 Shuhei Watanabe. Tree-structured parzen estimator: Understanding its algorithm components and
725 their roles for better empirical performance. *arXiv preprint arXiv:2304.11127*, 2023.
- 726 Anthony R West. *Solid state chemistry and its applications*. John Wiley & Sons, 2022.
- 727 Luhuan Wu, Brian Trippe, Christian Naeseth, David Blei, and John P Cunningham. Practical and
728 asymptotically exact conditional sampling in diffusion models. *Advances in Neural Information*
729 *Processing Systems*, 36, 2024.
- 730 Weihao Xia, Yulun Zhang, Yujiu Yang, Jing-Hao Xue, Bolei Zhou, and Ming-Hsuan Yang. Gan
731 inversion: A survey. *IEEE transactions on pattern analysis and machine intelligence*, 45(3):
732 3121–3138, 2022.
- 733 Tian Xie, Xiang Fu, Octavian-Eugen Ganea, Regina Barzilay, and Tommi S Jaakkola. Crystal
734 diffusion variational autoencoder for periodic material generation. In *The Tenth International*
735 *Conference on Learning Representations*, 2022.
- 736 Keqiang Yan, Yi Liu, Yuchao Lin, and Shuiwang Ji. Periodic graph transformers
737 for crystal material property prediction. In S. Koyejo, S. Mohamed, A. Agarwal,
738 D. Belgrave, K. Cho, and A. Oh (eds.), *Advances in Neural Information Process-*
739 *ing Systems*, volume 35, pp. 15066–15080. Curran Associates, Inc., 2022. URL
740 [https://proceedings.neurips.cc/paper_files/paper/2022/file/
6145c70a4a4bf353a31ac5496a72a72d-Paper-Conference.pdf](https://proceedings.neurips.cc/paper_files/paper/2022/file/6145c70a4a4bf353a31ac5496a72a72d-Paper-Conference.pdf).
- 741 Han Yang, Chenxi Hu, Yichi Zhou, Xixian Liu, Yu Shi, Jielan Li, Guanzhi Li, Zekun Chen,
742 Shuizhou Chen, Claudio Zeni, et al. Mattersim: A deep learning atomistic model across ele-
743 ments, temperatures and pressures. *arXiv preprint arXiv:2405.04967*, 2024a.
- 744 Jiaqi Yang and Arun Mannodi-Kanakkithodi. High-throughput computations and machine learning
745 for halide perovskite discovery. *MRS Bulletin*, 47(9):940–948, 2022.
- 746 Sherry Yang, KwangHwan Cho, Amil Merchant, Pieter Abbeel, Dale Schuurmans, Igor Mordatch,
747 and Ekin Dogus Cubuk. Scalable diffusion for materials generation. In *The Twelfth Interna-*
748 *tional Conference on Learning Representations*, 2024b. URL [https://openreview.net/
749 forum?id=wm4WlHoXpC](https://openreview.net/forum?id=wm4WlHoXpC).

756 Chengxuan Ying, Tianle Cai, Shengjie Luo, Shuxin Zheng, Guolin Ke, Di He, Yanming Shen,
757 and Tie-Yan Liu. Do transformers really perform badly for graph representation? In
758 M. Ranzato, A. Beygelzimer, Y. Dauphin, P.S. Liang, and J. Wortman Vaughan (eds.), *Ad-
759 vances in Neural Information Processing Systems*, volume 34, pp. 28877–28888. Curran
760 Associates, Inc., 2021. URL [https://proceedings.neurips.cc/paper_files/
761 paper/2021/file/f1c1592588411002af340cbaedd6fc33-Paper.pdf](https://proceedings.neurips.cc/paper_files/paper/2021/file/f1c1592588411002af340cbaedd6fc33-Paper.pdf).

762 Claudio Zeni, Robert Pinsler, Daniel Zügner, Andrew Fowler, Matthew Horton, Xiang Fu, Sasha
763 Shysheya, Jonathan Crabbé, Lixin Sun, Jake Smith, et al. Mattergen: a generative model for
764 inorganic materials design. *arXiv preprint arXiv:2312.03687*, 2023.

765 Hanfeng Zhai, Hongxia Hao, and Jingjie Yeo. Benchmarking inverse optimization algorithms for
766 materials design. *APL Materials*, 12(2), 2024.

767
768
769
770
771
772
773
774
775
776
777
778
779
780
781
782
783
784
785
786
787
788
789
790
791
792
793
794
795
796
797
798
799
800
801
802
803
804
805
806
807
808
809

A APPENDIX

A.1 DETAILS OF THE SETTINGS IN DENSITY FUNCTIONAL THEORY

We used Density Functional Theory (DFT) to verify the band gaps of materials proposed by SMOACS. We employed the Vienna Ab initio Simulation Package (VASP) (Kresse & Joubert, 1999) version 5.4.4 with Perdew-Burke-Ernzerhof (PBE) exchange-correlation functional (Perdew et al., 1996) and Projector Augmented Wave (PAW) pseudo-potentials (Blöchl, 1994) in all DFT calculations. We used the MPRelaxSet from PyMatGen (Ong et al., 2013) to generate input files: KPOINTS and INCAR.

A.2 BAND GAP DISCREPANCIES BETWEEN MACHINE LEARNING PREDICTED AND DFT CALCULATED

SMOACS heavily relies on the accuracy of property prediction models. However, we found discrepancies between the values model predicted and the DFT calculated (Fig.A.1). Furthermore, structures relaxed by the MPRelaxSet, which is a parameter set for structural relaxations with VASP provided in PyMatGen, sometimes significantly differ from their proposed forms. There are two possible reasons. First, DFT settings: MEGNet dataset comes from an older version of Materials Project database (Jain et al., 2013). Materials in this database are sometimes updated, and calculation conditions when the MEGNet dataset is created could be different from the current MPRelaxset. We could not reproduce the band gap values in the MEGNet dataset with MPRelaxset. Second, MEGNet dataset features: All models used in this work are trained on the MEGNet dataset, which is comprised predominantly of stable materials. So, predicting unstable or physically inappropriate structures with these models can lead to inaccurate predictions that may affect the proposed materials. To address these issues, we may need a model trained on a large dataset that includes both stable and unstable structures.

The MEGNet dataset utilizes DFT calculations with PBE functionals that are known to underestimate band gaps. Consequently, when models trained on the MEGNet dataset are used in SMOACS, this tendency may be reflected in the predictions of the proposed materials. This issue may be addressed by constructing a dataset using more accurate band gap calculations, such as HSE06 hybrid functionals (Krukau et al., 2006) and adopting models trained on that dataset. It should be noted that the amount of data available with these accurate calculations is much more limited than for DFT-PBE.

A.3 A POSSIBLE APPLICATION: IDENTIFYING THE MOST STABLE CRYSTAL STRUCTURE

Our method can optimize energy while specifying the base crystal structure. This property may allow for identifying crystal structures based either solely on the chemical formula or on a combination of the chemical formula and physical properties. This is a Crystal Structure Prediction (CSP) task (Ryan et al., 2018; Miller et al., 2024; Jiao et al., 2024). To verify if this is possible, we experimented to see if the crystal structure of metallic silicon with a zero band gap could be identified. Initially, we extracted structures from the MEGNet dataset that contained only one atom besides Si, using them as the initial structure. The atomic distribution was fixed with a one-hot vector indicating silicon, and only the lattice constants were optimized. The target properties for optimization were a zero band gap and formation energy minimization. We chose silicon structures from the MEGNet dataset with a band gap of 0 eV as the reference and compared these with the optimized structures that exhibited the lowest formation energy. Consequently, we identified structures close to the reference among those optimized for the lowest formation energy.

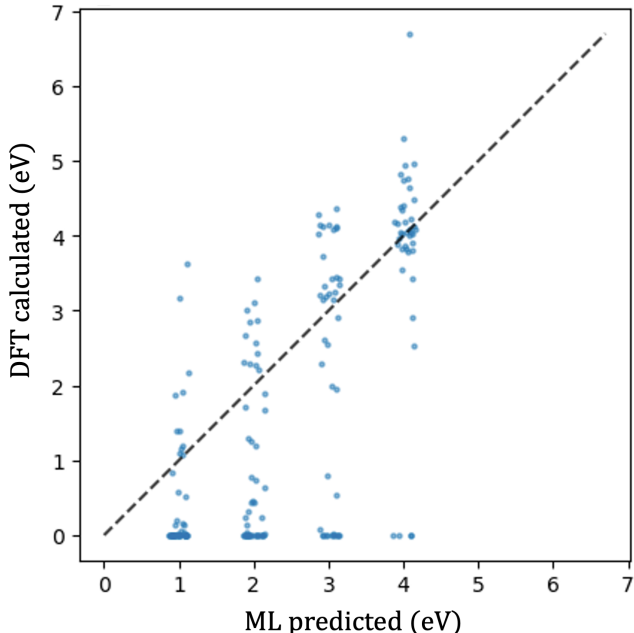
The results are shown in Table A.1. The reference material of mp-34 is close to optimized candidate No. 2. Similarly, mp-1014212 is close to candidates from No. 4 to No. 12.”

A.4 IMPLEMENTATION DETAILS

To demonstrate that SMOACS can utilize various property prediction models, we selected ALIGNN as a representative of the GNN-based models and Crystalformer as a representative of the

864
865
866
867
868
869
870
871
872
873
874
875
876
877
878
879
880
881
882
883
884
885
886

Band gap discrepancies between DFT and ML



887 Figure A.1: The discrepancies between band gap values predicted the machine learning model
888 (Crystalformer) and that of DFT calculated.

889

Table A.1: Reference Si materials (band gap 0 eV) and optimized candidates.

891
892
893
894
895
896
897
898
899
900
901
902
903
904
905
906
907
908
909

Materials	a, b, c (Å)	α, β, γ (°)	predicted formation energy (eV)
(Ref) mp-34	2.64, 2.64, 2.47	90.0, 90.0, 120	-
(Ref) mp-1014212	2.66, 2.66, 2.66	109.5, 109.5, 109.5	-
candidate-1	2.67, 2.67, 2.94	124.0, 124.0, 97.9	-0.367
candidate-2	2.50, 2.50, 2.27	89.9, 89.9, 134.0	-0.359
candidate-3	2.76, 2.76, 2.76	115.3, 115.3, 115.3	-0.326
candidate-4	2.72, 2.72, 2.72	115.0, 115.0, 115.0	-0.310
candidate-5	2.71, 2.71, 2.71	114.9, 114.9, 114.9	-0.310
candidate-6	2.71, 2.71, 2.71	114.9, 114.9, 114.9	-0.310
candidate-7	2.71, 2.71, 2.71	114.9, 114.9, 114.9	-0.308
candidate-8	2.73, 2.73, 2.73	115.0, 115.0, 115.0	-0.308
candidate-9	2.69, 2.69, 2.69	114.9, 114.9, 114.9	-0.308
candidate-10	2.68, 2.68, 2.68	114.8, 114.8, 114.8	-0.304
candidate-11	2.64, 2.64, 2.64	114.3, 114.3, 114.3	-0.266
candidate-12	2.55, 2.55, 2.55	113.9, 113.9, 113.9	-0.263
candidate-13	2.44, 2.43, 2.44	68.8, 64.7, 111.1	-0.243
candidate-14	2.42, 2.42, 2.42	112.3, 112.3, 112.3	-0.239
candidate-15	2.42, 2.42, 2.42	112.3, 112.3, 112.3	-0.239

910
911
912
913
914
915
916
917

Transformer-based models. For both ALIGNN and Crystalformer, we utilized publicly available weights trained on the MEGNet dataset that predict band gaps and formation energies.

The number of optimization steps was 200 for both SMOACS and TPE. The softmax temperature T was linearly decayed from $T = 0.01$ at step 1 to $T = 0.0001$ at step 200. Unless otherwise specified, to prevent extreme crystal structures, the crystal axis lengths a, b, c were clipped to a range of 2 Å to 10 Å, and the angles α, β, γ were clipped to between 30° and 150°. The types of elements considered ranged from atomic numbers 1 to 98. Unless otherwise noted, the search range

918 for TPE was aligned with SMOACS, with crystal axis lengths a, b, c ranging from 2 Å to 10 Å and
 919 angles α, β, γ from 30° to 150°. We set the strength parameter $\lambda = 1.0$.
 920

921 In ALIGNN, bonds are defined using a graph structure. However, because the graph structure is
 922 non-differentiable, it cannot be optimized directly. Moreover, as the crystal structure is optimized,
 923 the nearest-neighbor atoms may change, potentially rendering the continued use of the same graph
 924 structure inappropriate. Therefore, we updated the graph structure multiple times during the opti-
 925 mization process. Considering that the learning rate decay follows a cosine schedule, we updated
 926 the graph several times according to a sine schedule, which is the integral of the cosine function.

927 SMOACS was implemented using PyTorch (Paszke et al., 2019); we used the web-available imple-
 928 mentation of FTCP¹ and trained it on the MEGNet dataset. Optuna (Akiba et al., 2019) was used for
 929 TPE. We conducted optimizations using ALIGNN and Crystalformer, GNN-based, and transformer-
 930 based models, respectively. We used a NVIDIA A100 GPU. We utilized official codes and weights
 931 that are available online^{2,3}.

932 We trained FTCP from scratch using the MEGNet dataset. We tuned the hyperparameters, including
 933 the `max_elms` parameter (the number of types of atoms in the crystal), the `max_sites` param-
 934 eter (the number of atomic sites in the crystal), and the learning rate. As a result, `max_elms`,
 935 `max_sites`, and the learning rate were set to 4, 20, and 0.0001, respectively. Note that the MEG-
 936 Net dataset contains data with a larger number of element types and sites than these settings, so we
 937 did not utilize all 60,000 training samples; however, the reconstruction error score was better with
 938 this setting. During inference, after testing several values for the standard deviation of the noise
 939 added to the latent variables, we decided to sample from a normal distribution with a mean of 0 and
 940 a standard deviation of 0.6.

941 A.5 APPLICABILITY TO PROPERTY PREDICTION MODELS

942 This strategy of using atomic distributions discussed in Section 3 is widely applicable to various
 943 property prediction models. It readily supports formats such as Crystalformer, where one-hot vectors
 944 representing elements are fed into the model. Next, we consider a scenario of using models such as
 945 ALIGNN that require atomic representations as input. In this scenario, we treat the inner product
 946 of the atomic distribution \mathbf{a}_n and the u -dimensional representation vector for atoms \mathbf{r}_{atom} ($\mathbf{r}_{\text{atom}} \in$
 947 $\mathbb{R}^{K \times u}$) as the atomic representation. In either case, since the output is connected to the learnable
 948 atomic distributions through the chain rule of differentiation, we are able to optimize the atomic
 949 distribution through backpropagation.
 950

951 A.6 DETAILS IN SIMULTANEOUS OPTIMIZATION OF TARGETED PROPERTIES REGARDLESS 952 OF THE CRYSTAL STRUCTURE

953 We optimized the band gap regardless of the crystal structure and simultaneously minimized the
 954 formation energy. We randomly selected initial crystal structures with up to 10 atomic sites from
 955 the MEGNet dataset for SMOACS and TPE, ensuring that each selected structure met the crite-
 956 rion of electrical neutrality. In SMOACS, we selected up to 10 possible oxidation number pat-
 957 terns based on the atom combinations in the initial crystal structure, all of which ensure overall
 958 electrical neutrality. the learning rates were set as $\eta_l = 0.01, \eta_C = 0.02, \eta_A = \eta_O = 6.0$
 959 for SMOACS with Crystalformer. For SMOACS with ALIGNN, the learning rates were set as
 960 $\eta_l = 0.008, \eta_C = 0.02, \eta_A = \eta_O = 0.0002$. The learning rates were decayed using a cosine
 961 annealing schedule.
 962

963 We updated the graph structure data in ALIGNN 32 times according to a sine schedule, which is
 964 the integral of the cosine function. Specifically, we reconstructed the graph structure based on the
 965 current crystal configuration at steps [4, 8, 12, 16, 20, 24, 28, 32, 36, 40, 44, 48, 52, 56, 61, 65, 69,
 966 74, 79, 83, 88, 93, 99, 104, 110, 116, 123, 129, 137, 146, 156, 169], as well as during the evalua-
 967 tion after optimization. Then, we constructed masks \mathbf{M}_d corresponding to its oxidation pattern d .
 968 The atomic distribution \mathbf{A} and the oxidation state configuration parameter \mathbf{o} were initialized with
 969 a uniform distribution. The loss functions for the band gap and formation energy in SMOACS use

970 ¹<https://github.com/PV-Lab/FTCP>

971 ²<https://github.com/usnistgov/alignn>

³<https://github.com/omron-sinicx/crystalformer>

Equation 14. TPE required separate settings for each objective: band gap, formation energy, and electrical neutrality. The objectives for band gap and formation energy were adopted from Equation 13. Additionally, we implemented a binary objective function that assigns a value of 0 if electrical neutrality is achieved and 1 otherwise:

$$L_{\text{neutral}} = \begin{cases} 0 & \text{electrical neutrality} \\ 1 & \text{otherwise} \end{cases} \quad (\text{A.1})$$

TPE used L_{bg} , L_f and L_{neutral} as objective functions, respectively. FTCP selects initial data from the training dataset where the band gap is close to the target and the formation energy is below -0.5 eV, and then uses an encoder to convert this into latent variables. Next, we add noise to these latent variables using a normal distribution with a mean of 0 and a standard deviation of 0.6, then decode them back into crystal structures for evaluation. Augmented results are shown in Table A.2. We also evaluate the diversity of the proposed materials, as shown in Table A.3.

SMOACS consistently maintained electrical neutrality, provided that extreme geometries causing NaN values during crystal vector calculations did not occur. We calculate the crystal vectors from a , b , c , and α , β , γ . When the crystal axis lengths or angles are extremely large, computational errors can cause the value under the square root to become a very small negative number, resulting in NaN occurrences. Apart from this, SMOACS consistently maintained electrical neutrality. SMOACS utilizing ALIGNN achieved significantly lower scores compared to when using Crystalformer. We attribute this to the optimization difficulty arising from changes in the shape of the hypersurface of the loss function due to updates to the graph structure. SMOACS demonstrates the ability to generate highly diverse materials.

1026
1027
1028
1029
1030
1031
1032
1033
1034
1035
1036
1037
1038
1039
1040
1041
1042
1043
1044
1045
1046
1047
1048
1049
1050
1051
1052
1053
1054
1055
1056
1057
1058
1059
1060
1061
1062
1063
1064
1065
1066
1067
1068
1069
1070
1071
1072
1073
1074
1075
1076
1077
1078
1079

Table A.2: Experiments on optimizing for various targets of a band gap. The "success rate" is the probability of simultaneously satisfying three conditions: (A) the band gap is optimized within the target range, (B) the formation energy is below -0.5 eV, and (C) the crystal structure is valid. C is achieved when two criteria are met simultaneously: (a) all interatomic distances are greater than 0.5 Å, and (b) the structure is electrically neutral. S(Cry) and S(ALI) denote SMOACS utilizing the Crystalformer and ALIGNN models, respectively. We evaluate each of the proposed materials using all evaluation metrics, and the results are averaged over 256 samples. Higher scores are better across all metrics.

Target BG (eV)	method	success rate	(A)BG	(B) E_f	(C)STR	(a) neut	(b) 0.5Å
0.50 ± 0.04	S(Cry)	0.328	0.465	0.566	0.758	0.957	0.758
	S(ALI)	0.055	0.062	0.867	0.867	0.949	0.867
	TPE	0.004	0.945	0.059	0.066	0.070	0.910
	FTCP	0.000	0.004	1.000	0.719	0.746	0.906
1.00 ± 0.04	S(Cry)	0.340	0.504	0.613	0.785	0.973	0.785
	S(ALI)	0.047	0.059	0.848	0.805	0.926	0.805
	TPE	0.016	0.934	0.066	0.070	0.070	0.891
	FTCP	0.004	0.004	1.000	0.699	0.730	0.891
1.50 ± 0.04	S(Cry)	0.387	0.543	0.672	0.824	0.980	0.824
	S(ALI)	0.043	0.066	0.828	0.852	0.938	0.852
	TPE	0.020	0.855	0.055	0.074	0.082	0.828
	FTCP	0.000	0.000	1.000	0.703	0.723	0.895
2.00 ± 0.04	S(Cry)	0.355	0.484	0.703	0.844	0.988	0.844
	S(ALI)	0.082	0.092	0.820	0.838	0.914	0.838
	TPE	0.020	0.789	0.062	0.086	0.086	0.812
	FTCP	0.000	0.000	1.000	0.699	0.727	0.895
2.50 ± 0.04	S(Cry)	0.383	0.473	0.715	0.840	0.984	0.840
	S(ALI)	0.051	0.059	0.809	0.793	0.898	0.793
	TPE	0.023	0.711	0.098	0.051	0.055	0.816
	FTCP	0.004	0.004	1.000	0.695	0.707	0.902
3.00 ± 0.04	S(Cry)	0.301	0.375	0.699	0.828	0.992	0.828
	S(ALI)	0.039	0.043	0.801	0.820	0.906	0.820
	TPE	0.020	0.645	0.094	0.090	0.098	0.766
	FTCP	0.027	0.031	1.000	0.668	0.680	0.902
3.50 ± 0.04	S(Cry)	0.188	0.273	0.645	0.750	0.992	0.750
	S(ALI)	0.016	0.016	0.816	0.797	0.902	0.797
	TPE	0.012	0.586	0.059	0.055	0.059	0.730
	FTCP	0.012	0.012	1.000	0.707	0.730	0.883
4.00 ± 0.04	S(Cry)	0.160	0.227	0.656	0.789	1.000	0.789
	S(ALI)	0.023	0.023	0.805	0.797	0.902	0.797
	TPE	0.016	0.438	0.090	0.078	0.078	0.680
	FTCP	0.035	0.043	1.000	0.676	0.691	0.895

1080
 1081
 1082
 1083
 1084
 1085
 1086
 1087
 1088
 1089
 1090
 1091
 1092
 1093
 1094
 1095
 1096
 1097
 1098
 1099
 1100
 1101
 1102
 1103
 1104
 1105
 1106
 1107
 1108
 1109
 1110
 1111
 1112
 1113
 1114
 1115
 1116
 1117
 1118
 1119
 1120
 1121
 1122
 1123
 1124
 1125
 1126
 1127
 1128
 1129
 1130
 1131
 1132
 1133

Table A.3: The diversity of the proposed materials. The 'success rate' corresponds to the same 'success rate' as in Table A.2. The 'unique rate' refers to the probability of materials with unique elemental combinations, regardless of the success. The 'unique rate in success' represents the proportion of materials with unique elemental combinations among the successfully optimized materials. The 'unique and novel rate in success' indicates the proportion of materials whose elemental combinations are unique and absent from the MEGNet database among the successfully optimized materials.

Target BG (eV)	method	success rate	unique rate	unique rate in success	unique and novel rate in success
0.50 ±0.04	S(Cry)	0.328	0.957	84/84	81/84
	S(ALI)	0.055	0.867	14/14	13/14
	TPE	0.004	1.000	1/1	0/1
	FTCP	0.000	0.297	-	-
1.00 ±0.04	S(Cry)	0.340	0.973	87/87	80/87
	S(ALI)	0.047	0.895	12/12	11/12
	TPE	0.016	1.000	4/4	1/4
	FTCP	0.004	0.289	1/1	0/1
1.50 ±0.04	S(Cry)	0.387	0.977	99/99	94/99
	S(ALI)	0.043	0.891	11/11	11/11
	TPE	0.020	1.000	5/5	0/5
	FTCP	0.000	0.324	-	-
2.00 ±0.04	S(Cry)	0.355	0.984	90/91	85/91
	S(ALI)	0.082	0.836	42/42	41/42
	TPE	0.020	1.000	5/5	1/5
	FTCP	0.000	0.328	-	-
2.50 ±0.04	S(Cry)	0.383	0.980	98/98	90/98
	S(ALI)	0.051	0.793	13/13	12/13
	TPE	0.023	1.000	6/6	1/6
	FTCP	0.004	0.328	1/1	0/1
3.00 ±0.04	S(Cry)	0.301	0.992	77/77	72/77
	S(ALI)	0.039	0.770	9/10	6/10
	TPE	0.020	0.992	4/5	2/5
	FTCP	0.027	0.359	6/7	0/7
3.50 ±0.04	S(Cry)	0.188	0.992	48/48	47/48
	S(ALI)	0.016	0.793	4/4	4/4
	TPE	0.012	1.000	3/3	1/3
	FTCP	0.012	0.309	3/3	0/3
4.00 ±0.04	S(Cry)	0.160	0.996	41/41	38/41
	S(ALI)	0.023	0.797	6/6	6/6
	TPE	0.016	0.996	4/4	1/4
	FTCP	0.035	0.348	7/9	0/9

A.7 DETAILS IN SIMULTANEOUS OPTIMIZATION OF TARGETED PROPERTIES WHILE PRESERVING PEROVSKITE STRUCTURES

As discussed in Section 3.3, due to the arbitrariness in the numerical values of the lattice constant and coordinates of perovskite structures, we evaluated whether the optimized structures approximated typical perovskite configurations. First of all, fractional coordinates typical of perovskite structures are as follows: (0.5, 0.5, 0.5) at the A site, (0.0, 0.0, 0.0) at the B site, and (0.5, 0.0, 0.0), (0.0, 0.5, 0.0), (0.0, 0.0, 0.5) at the three X sites. We established criteria for the optimized x, y, and z coordinates to be within a deviation ϵ from these standard values. The perovskite structure $\text{CaCu}_3\text{Ti}_4\text{O}_{12}$ exhibits a slightly distorted configuration, with the x-coordinate of the oxygen atoms deviating by approximately 10% from their typical positions (Božin et al., 2004). To explore new structures, we set $\epsilon = 0.15$, allowing for a slightly greater distortion. We considered the optimized coordinates successful if the x, y, and z coordinates of each site fell within $\pm\epsilon$. Additionally, the angles between the crystal axes of typical perovskite structures are close to 90° . Therefore, angles between 85° and 95° were established as a criterion.

Using t values from typical perovskite structures (BaCeO_3 : 0.857, SrTiO_3 : 0.910 and BaTiO_3 : 0.970), we established a tolerance factor range of $0.8 \leq t \leq 1.0$ as the criterion for success. The ionic radius of the X site was calculated as the average of the radii of the three X sites. We took the values for the ionic radii from PyMatGen (Ong et al., 2013).

In this experiments, the learning rates were set as $\eta_l = 0.01, \eta_C = 0.02, \eta_A = \eta_O = 6.0$ for SMOACS with Crystalformer. For SMOACS with ALIGNN, the learning rates were set as $\eta_l = 0.5, \eta_C = 0.002, \eta_A = \eta_O = 0.00008$. We reconstructed the graph structure 46 times during the optimizations. The learning rates were decayed using a cosine annealing schedule.

Due to the limited number of perovskite structure data points in the MEGNet dataset, we generated 256 random perovskite structures as initial values for SMOACS. These structures have crystal axis angles α, β , and γ at 90° and axis lengths a, b , and c randomly generated between 2 \AA and 10 \AA . Their initial fractional coordinates correspond to those typical of perovskite structures: (0.5, 0.5, 0.5) for the A site, (0.0, 0.0, 0.0) for the B site, and (0.5, 0.0, 0.0), (0.0, 0.5, 0.0), and (0.0, 0.0, 0.5) for the three X sites. Similarly, TPE optimized perovskite structures by setting the crystal axis angles at 90° and optimizing the axis lengths a, b, c between 2 \AA and 10 \AA . We also limited element species for each site in TPE. Specifically, the elements are restricted by oxidation numbers: +1 and +2 for site A, +2 and +4 for site B, and -1 and -2 for site X. For FTCP, we initially selected data points where the crystal axis angles were at 90° , and all sites conformed to the typical fractional coordinates of perovskite structures; these were then converted into latent variables. Subsequently, we applied noise using a normal distribution with a mean of 0 and a standard deviation of 0.6 to the latent variables. Finally, we decoded the latent variables back into crystal structures for evaluation.

SMOACS conducted optimization using Eq 17. For t , TPE used another objective function:

$$L_t^{\text{TPE}} = \begin{cases} 0 & (0.8 \leq t \leq 1.0) \\ 1 & \text{otherwise} \end{cases} \quad (\text{A.2})$$

TPE used $L_{\text{bg}}, L_f, L_{\text{neutral}}$ and L_t^{TPE} as objective functions, respectively. Augmented results are shown in Table A.4. We also evaluate the diversity of the proposed materials, as shown in Table A.5.

1188
 1189
 1190
 1191
 1192
 1193
 1194
 1195
 1196
 1197
 1198
 1199
 1200
 1201
 1202
 1203
 1204
 1205
 1206
 1207
 1208
 1209
 1210
 1211
 1212
 1213
 1214
 1215
 1216
 1217
 1218
 1219
 1220
 1221
 1222
 1223
 1224
 1225
 1226
 1227
 1228
 1229
 1230
 1231
 1232
 1233
 1234
 1235
 1236
 1237
 1238
 1239
 1240
 1241

Table A.4: Experiments on optimizing various band gaps while preserving perovskite structures. The "success rate" reflects the probability of simultaneously satisfying four criteria: (A) the band gap is optimized within the target range, (B) the formation energy is below -0.5 eV, (C) the crystal structure is valid, and (D) approximating a valid perovskite structure. Criteria (A), (B), and (C) are consistent with those outlined in Table 2. The (D) is achieved when three criteria are met simultaneously: (c) the tolerance factor t is between 0.8 and 1.0, (d) coordinates are within ± 0.15 of typical perovskite structure coordinates, and (e) axis angles are from 85° to 95° . We evaluate each of the proposed materials using all evaluation metrics, and the results are averaged over 256 samples. Higher scores are better across all metrics.

Target BG (eV)	method	success rate	(A)BG	(B) E_f	(C)STR _i	(a) neut	(b) 0.5Å	(D)PS	(c) tole	(d) angles	(e) coord
0.50 ±0.04	S(Cry)	0.113	0.477	0.410	0.965	1.000	0.965	0.500	0.500	1.000	1.000
	S(ALI)	0.090	0.211	0.535	1.000	1.000	1.000	0.500	0.500	1.000	1.000
	TPE	0.027	1.000	0.137	0.535	0.535	1.000	0.648	0.648	1.000	1.000
	FTCP	0.004	0.023	1.000	0.836	0.840	0.938	0.258	0.508	0.441	0.285
1.00 ±0.04	S(Cry)	0.152	0.457	0.422	0.961	1.000	0.961	0.559	0.559	1.000	1.000
	S(ALI)	0.062	0.168	0.484	1.000	1.000	1.000	0.531	0.531	1.000	1.000
	TPE	0.012	1.000	0.137	0.395	0.395	1.000	0.664	0.664	1.000	1.000
	FTCP	0.004	0.023	1.000	0.859	0.863	0.965	0.215	0.531	0.418	0.270
1.50 ±0.04	S(Cry)	0.148	0.422	0.461	0.984	1.000	0.984	0.578	0.578	1.000	1.000
	S(ALI)	0.070	0.219	0.652	1.000	1.000	1.000	0.629	0.629	1.000	1.000
	TPE	0.023	0.992	0.281	0.293	0.293	1.000	0.523	0.523	1.000	1.000
	FTCP	0.000	0.016	1.000	0.895	0.906	0.965	0.242	0.547	0.418	0.320
2.00 ±0.04	S(Cry)	0.188	0.426	0.516	0.988	1.000	0.988	0.613	0.613	1.000	1.000
	S(ALI)	0.090	0.188	0.980	1.000	1.000	1.000	0.625	0.625	1.000	1.000
	TPE	0.027	0.977	0.266	0.266	0.266	1.000	0.547	0.547	1.000	1.000
	FTCP	0.004	0.004	1.000	0.891	0.898	0.980	0.281	0.551	0.473	0.324
2.50 ±0.04	S(Cry)	0.152	0.285	0.516	0.988	1.000	0.988	0.625	0.625	1.000	1.000
	S(ALI)	0.113	0.184	0.938	1.000	1.000	1.000	0.625	0.625	1.000	1.000
	TPE	0.016	0.918	0.281	0.352	0.352	1.000	0.387	0.387	1.000	1.000
	FTCP	0.008	0.012	0.996	0.879	0.898	0.953	0.250	0.543	0.441	0.289
3.00 ±0.04	S(Cry)	0.102	0.219	0.508	0.992	1.000	0.992	0.621	0.621	1.000	1.000
	S(ALI)	0.141	0.273	0.938	1.000	1.000	1.000	0.625	0.625	1.000	1.000
	TPE	0.035	0.875	0.293	0.234	0.234	1.000	0.316	0.316	1.000	1.000
	FTCP	0.008	0.008	1.000	0.898	0.906	0.969	0.246	0.543	0.418	0.316
3.50 ±0.04	S(Cry)	0.070	0.145	0.516	0.996	1.000	0.996	0.629	0.629	1.000	1.000
	S(ALI)	0.176	0.195	0.961	1.000	1.000	1.000	0.668	0.668	1.000	1.000
	TPE	0.016	0.711	0.266	0.184	0.184	1.000	0.285	0.285	1.000	1.000
	FTCP	0.004	0.008	1.000	0.895	0.910	0.953	0.238	0.531	0.441	0.277
4.00 ±0.04	S(Cry)	0.051	0.094	0.512	0.992	1.000	0.992	0.625	0.625	1.000	1.000
	S(ALI)	0.180	0.285	0.961	1.000	1.000	1.000	0.605	0.605	1.000	1.000
	TPE	0.020	0.539	0.336	0.215	0.215	1.000	0.227	0.227	1.000	1.000
	FTCP	0.000	0.004	0.996	0.883	0.887	0.949	0.238	0.535	0.410	0.305

1242
 1243
 1244
 1245
 1246
 1247
 1248
 1249
 1250
 1251
 1252
 1253
 1254
 1255
 1256
 1257
 1258
 1259
 1260
 1261
 1262
 1263
 1264
 1265
 1266
 1267
 1268
 1269
 1270
 1271
 1272
 1273
 1274
 1275
 1276
 1277
 1278
 1279
 1280
 1281
 1282
 1283
 1284
 1285
 1286
 1287
 1288
 1289
 1290
 1291
 1292
 1293
 1294
 1295

Table A.5: The diversity of the proposed materials. The 'success rate' corresponds to the same 'success rate' as in Table A.4. The 'unique rate' refers to the probability of materials with unique elemental combinations, regardless of the success. The 'unique rate in success' represents the proportion of materials with unique elemental combinations among the successfully optimized materials. The 'unique and novel rate in success' indicates the proportion of materials whose elemental combinations are unique and absent from the MEGNet database among the successfully optimized materials.

Target BG (eV)	method	success rate	unique rate	unique rate in success	unique and novel rate in success
0.50 ±0.04	S(Cry)	0.113	0.898	28/29	27/29
	S(ALI)	0.090	0.398	14/23	13/23
	TPE	0.027	0.984	7/7	7/7
	FTCP	0.004	0.352	1/1	0/1
1.00 ±0.04	S(Cry)	0.152	0.891	38/39	37/39
	S(ALI)	0.062	0.562	14/16	12/16
	TPE	0.012	0.996	3/3	3/3
	FTCP	0.004	0.336	1/1	0/1
1.50 ±0.04	S(Cry)	0.148	0.891	38/38	38/38
	S(ALI)	0.070	0.555	16/18	15/18
	TPE	0.023	1.000	6/6	6/6
	FTCP	0.000	0.285	-	-
2.00 ±0.04	S(Cry)	0.188	0.902	47/48	46/48
	S(ALI)	0.090	0.445	17/23	17/23
	TPE	0.027	0.996	7/7	7/7
	FTCP	0.004	0.309	1/1	0/1
2.50 ±0.04	S(Cry)	0.152	0.898	38/39	36/39
	S(ALI)	0.113	0.598	25/29	23/29
	TPE	0.016	0.992	4/4	4/4
	FTCP	0.008	0.309	2/2	0/2
3.00 ±0.04	S(Cry)	0.102	0.902	26/26	26/26
	S(ALI)	0.141	0.465	24/36	21/36
	TPE	0.035	0.992	9/9	9/9
	FTCP	0.008	0.285	2/2	0/2
3.50 ±0.04	S(Cry)	0.070	0.902	18/18	17/18
	S(ALI)	0.176	0.387	14/45	12/45
	TPE	0.016	0.988	4/4	4/4
	FTCP	0.004	0.301	1/1	0/1
4.00 ±0.04	S(Cry)	0.051	0.902	13/13	13/13
	S(ALI)	0.180	0.387	20/46	14/46
	TPE	0.020	0.977	5/5	5/5
	FTCP	0.000	0.312	-	-

A.8 DETAILS IN OPTIMIZING LARGE ATOMIC CONFIGURATIONS

We conducted experiments on $3 \times 3 \times 3$ perovskite structures containing 135 atom sites, expanded from a unit cell with five atom sites. As the cell size increased, the range for the crystal lattice dimensions a, b, c in SMOACS and TPE was set from 6 Å to 30 Å for the $3 \times 3 \times 3$ structure. Similarly, the range of coordinate variations ϵ was set to 0.05. Aside from these changes, the experimental conditions remained consistent with those described in Section 4.3. In this experiments, the learning rates were set as $\eta_l = 0.003, \eta_C = 0.005, \eta_A = \eta_O = 2.0$ for SMOACS with Crystalformer. For SMOACS with ALIGNN, the learning rates were set as $\eta_l = 5.000, \eta_C = 0.002, \eta_A = \eta_O = 0.00005$. We reconstructed the graph structure 41 times during the optimizations. The learning rates were decayed using a cosine annealing schedule. Augmented results are shown in Table A.6.

Table A.6: Experiments optimizing for various band gaps while preserving a $3 \times 3 \times 3$ perovskite structure. We included only TPE, which showed better performance in Section 4.3, for comparison. Evaluation methods are based on those described in Table 3.

Target BG (eV)	method	success rate	(A)BG	(B) E_f	(C)STR	(a) neut	(b) 0.5Å	(D)PS	(c) tole	(d) angles	(e) coord
0.50 ± 0.04	S(Cry)	0.156	0.734	0.547	0.968	1.00	0.969	0.570	0.570	1.000	1.000
	S(ALI)	0.188	0.234	0.812	0.687	1.00	0.688	0.789	0.789	1.000	1.000
	TPE(/N)	0.000	1.000	0.000	-	N/A	1.000	0.609	0.609	1.000	1.000
1.00 ± 0.04	S(Cry)	0.070	0.250	0.469	0.945	1.00	0.945	0.586	0.586	1.000	1.000
	S(ALI)	0.094	0.133	0.828	0.703	1.00	0.703	0.625	0.625	1.000	1.000
	TPE(/N)	0.000	0.125	0.000	-	N/A	0.992	0.242	0.242	1.000	1.000
1.50 ± 0.04	S(Cry)	0.047	0.125	0.422	0.953	1.00	0.953	0.617	0.617	1.000	1.000
	S(ALI)	0.062	0.086	0.867	0.726	1.00	0.727	0.586	0.586	1.000	1.000
	TPE(/N)	0.000	0.141	0.000	-	N/A	1.000	0.180	0.180	1.000	1.000
2.00 ± 0.04	S(Cry)	0.023	0.055	0.406	0.976	1.00	0.977	0.633	0.633	1.000	1.000
	S(ALI)	0.055	0.102	1.000	0.710	1.00	0.711	0.594	0.594	1.000	1.000
	TPE(/N)	0.000	0.125	0.000	-	N/A	0.984	0.242	0.242	1.000	1.000
2.50 ± 0.04	S(Cry)	0.023	0.039	0.438	0.984	1.00	0.984	0.664	0.664	1.000	1.000
	S(ALI)	0.102	0.172	1.000	0.703	1.00	0.703	0.812	0.812	1.000	1.000
	TPE(/N)	0.000	0.023	0.000	-	N/A	0.984	0.156	0.156	1.000	1.000
3.00 ± 0.04	S(Cry)	0.016	0.047	0.602	1.00	1.00	1.000	0.383	0.383	1.000	1.000
	S(ALI)	0.125	0.188	0.992	0.726	1.00	0.727	0.664	0.664	1.000	1.000
	TPE(/N)	0.000	0.023	0.000	-	N/A	0.984	0.273	0.273	1.000	1.000
3.50 ± 0.04	S(Cry)	0.008	0.008	0.445	0.984	1.00	0.984	0.672	0.672	1.000	1.000
	S(ALI)	0.156	0.250	1.000	0.75	1.00	0.750	0.734	0.734	1.000	1.000
	TPE(/N)	0.000	0.000	0.000	-	N/A	0.992	0.195	0.195	1.000	1.000
4.00 ± 0.04	S(Cry)	0.008	0.008	0.445	0.984	1.00	0.984	0.672	0.672	1.000	1.000
	S(ALI)	0.219	0.305	1.000	0.773	1.00	0.773	0.852	0.852	1.000	1.000
	TPE(/N)	0.000	0.000	0.000	-	N/A	0.969	0.180	0.180	1.000	1.000

A.9 ELECTRICAL NEUTRALITY

In assessing electrical neutrality, a compound was considered neutral if the sum of the oxidation numbers for the atoms at each site equaled zero. For example, Fe_3O_4 is electrically neutral because the configuration [Fe, Fe, Fe, O, O, O, O] can assume oxidation numbers of [+2, +3, +3, -2, -2, -2, -2] that sum to zero. Previous study (Xie et al., 2022) employed SMACT (Davies et al., 2019) to assess electrical neutrality; however, SMACT includes some oxidation numbers, like the +7 state of chlorine, which are extremely rare and potentially less reliable. We restricted our analysis to commonly occurring oxidation numbers, selecting those found at the intersection of SMACT and PyMatGen. A list of the elements and their corresponding oxidation numbers employed in this study is shown in Table A.7, Table A.8, and Table A.9. In these tables, the 'SMACT' indicates oxidation numbers from `smact.Element`. The 'icsd' and 'common' indicate oxidation numbers from `icsd_oxidation_state` and `common_oxidation_states` in `pymatgen.core.periodic_table.Element`, respectively. 'Ours' represents the oxidation numbers we used in this paper.

Table A.7: The List of oxidation numbers from Hydrogen (H) to Krypton (Kr).

Z	Elm	SMACT	icsd	common	Ours
1	H	{-1, 1}	{-1, 1}	{-1, 1}	{-1, 1}
2	He	{}	{}	{}	{}
3	Li	{1}	{1}	{1}	{1}
4	Be	{1, 2}	{2}	{2}	{2}
5	B	{1, 2, 3}	{-3, 3}	{3}	{3}
6	C	{-4, -3, -2, -1, 1, 2, 3, 4}	{-4, -3, -2, 2, 3, 4}	{-4, 4}	{-4, 4}
7	N	{-3, -2, -1, 1, 2, 3, 4, 5}	{-3, -2, -1, 1, 3, 5}	{-3, 3, 5}	{-3, 3, 5}
8	O	{-2, -1, 1, 2}	{-2}	{-2}	{-2}
9	F	{-1}	{-1}	{-1}	{-1}
10	Ne	{}	{}	{}	{}
11	Na	{-1, 1}	{1}	{1}	{1}
12	Mg	{1, 2}	{2}	{2}	{2}
13	Al	{1, 2, 3}	{3}	{3}	{3}
14	Si	{-4, -3, -2, -1, 1, 2, 3, 4}	{-4, 4}	{-4, 4}	{-4, 4}
15	P	{-3, -2, -1, 1, 2, 3, 4, 5}	{-3, -2, -1, 3, 4, 5}	{-3, 3, 5}	{-3, 3, 5}
16	S	{-2, -1, 1, 2, 3, 4, 5, 6}	{-2, -1, 2, 4, 6}	{-2, 2, 4, 6}	{-2, 2, 4, 6}
17	Cl	{-1, 1, 2, 3, 4, 5, 6, 7}	{-1}	{-1, 1, 3, 5, 7}	{-1}
18	Ar	{}	{}	{}	{}
19	K	{-1, 1}	{1}	{1}	{1}
20	Ca	{1, 2}	{2}	{2}	{2}
21	Sc	{1, 2, 3}	{2, 3}	{3}	{3}
22	Ti	{-1, 1, 2, 3, 4}	{2, 3, 4}	{4}	{4}
23	V	{-1, 1, 2, 3, 4, 5}	{2, 3, 4, 5}	{5}	{5}
24	Cr	{-2, -1, 1, 2, 3, 4, 5, 6}	{2, 3, 4, 5, 6}	{3, 6}	{3, 6}
25	Mn	{-3, -2, -1, 1, 2, 3, 4, 5, 6, 7}	{2, 3, 4, 7}	{2, 4, 7}	{2, 4, 7}
26	Fe	{-2, -1, 1, 2, 3, 4, 5, 6}	{2, 3}	{2, 3}	{2, 3}
27	Co	{-1, 1, 2, 3, 4, 5}	{1, 2, 3, 4}	{2, 3}	{2, 3}
28	Ni	{-1, 1, 2, 3, 4}	{1, 2, 3, 4}	{2}	{2}
29	Cu	{1, 2, 3, 4}	{1, 2, 3}	{2}	{2}
30	Zn	{1, 2}	{2}	{2}	{2}
31	Ga	{1, 2, 3}	{2, 3}	{3}	{3}
32	Ge	{-4, -3, -2, -1, 1, 2, 3, 4}	{2, 3, 4}	{-4, 2, 4}	{2, 4}
33	As	{-3, 1, 2, 3, 5}	{-3, -2, -1, 2, 3, 5}	{-3, 3, 5}	{-3, 3, 5}
34	Se	{-2, 1, 2, 4, 6}	{-2, -1, 4, 6}	{-2, 2, 4, 6}	{-2, 4, 6}
35	Br	{-1, 1, 2, 3, 4, 5, 7}	{-1, 5}	{-1, 1, 3, 5, 7}	{-1, 5}
36	Kr	{2}	{}	{}	{}

Table A.8: The List of oxidation numbers from Rubidium (Rb) to Radon (Rn).

Z	Elm	SMACT	icsd	common	Ours
37	Rb	{-1, 1}	{1}	{1}	{1}
38	Sr	{1, 2}	{2}	{2}	{2}
39	Y	{1, 2, 3}	{3}	{3}	{3}
40	Zr	{1, 2, 3, 4}	{2, 3, 4}	{4}	{4}
41	Nb	{-1, 1, 2, 3, 4, 5}	{2, 3, 4, 5}	{5}	{5}
42	Mo	{-2, -1, 1, 2, 3, 4, 5, 6}	{2, 3, 4, 5, 6}	{4, 6}	{4, 6}
43	Tc	{-3, -1, 1, 2, 3, 4, 5, 6, 7}	{}	{4, 7}	{}
44	Ru	{-2, 1, 2, 3, 4, 5, 6, 7, 8}	{2, 3, 4, 5, 6}	{3, 4}	{3, 4}
45	Rh	{-1, 1, 2, 3, 4, 5, 6}	{3, 4}	{3}	{3}
46	Pd	{1, 2, 4, 6}	{2, 4}	{2, 4}	{2, 4}
47	Ag	{1, 2, 3, 4}	{1, 2, 3}	{1}	{1}
48	Cd	{1, 2}	{2}	{2}	{2}
49	In	{1, 2, 3}	{1, 2, 3}	{3}	{3}
50	Sn	{-4, 2, 4}	{2, 3, 4}	{-4, 2, 4}	{2, 4}
51	Sb	{-3, 3, 5}	{-3, -2, -1, 3, 5}	{-3, 3, 5}	{-3, 3, 5}
52	Te	{-2, 2, 4, 5, 6}	{-2, -1, 4, 6}	{-2, 2, 4, 6}	{-2, 4, 6}
53	I	{-1, 1, 3, 4, 5, 7}	{-1, 5}	{-1, 1, 3, 5, 7}	{-1, 5}
54	Xe	{1, 2, 4, 6, 8}	{}	{}	{}
55	Cs	{-1, 1}	{1}	{1}	{1}
56	Ba	{2}	{2}	{2}	{2}
57	La	{2, 3}	{2, 3}	{3}	{3}
58	Ce	{2, 3, 4}	{3, 4}	{3, 4}	{3, 4}
59	Pr	{2, 3, 4}	{3, 4}	{3}	{3}
60	Nd	{2, 3, 4}	{2, 3}	{3}	{3}
61	Pm	{2, 3}	{}	{3}	{}
62	Sm	{2, 3}	{2, 3}	{3}	{3}
63	Eu	{2, 3}	{2, 3}	{2, 3}	{2, 3}
64	Gd	{1, 2, 3}	{3}	{3}	{3}
65	Tb	{1, 2, 3, 4}	{3, 4}	{3}	{3}
66	Dy	{2, 3, 4}	{3}	{3}	{3}
67	Ho	{2, 3}	{3}	{3}	{3}
68	Er	{2, 3}	{3}	{3}	{3}
69	Tm	{2, 3}	{3}	{3}	{3}
70	Yb	{2, 3}	{2, 3}	{3}	{3}
71	Lu	{3}	{3}	{3}	{3}
72	Hf	{2, 3, 4}	{4}	{4}	{4}
73	Ta	{-1, 1, 2, 3, 4, 5}	{3, 4, 5}	{5}	{5}
74	W	{-2, -1, 1, 2, 3, 4, 5, 6}	{2, 3, 4, 5, 6}	{4, 6}	{4, 6}
75	Re	{-3, -1, 1, 2, 3, 4, 5, 6, 7}	{3, 4, 5, 6, 7}	{4}	{4}
76	Os	{-2, -1, 1, 2, 3, 4, 5, 6, 7, 8}	{}	{4}	{}
77	Ir	{-3, -1, 1, 2, 3, 4, 5, 6, 7, 8}	{3, 4, 5}	{3, 4}	{3, 4}
78	Pt	{-2, -1, 1, 2, 3, 4, 5, 6}	{}	{2, 4}	{}
79	Au	{-1, 1, 2, 3, 5}	{}	{3}	{}
80	Hg	{1, 2, 4}	{1, 2}	{1, 2}	{1, 2}
81	Tl	{-1, 1, 3}	{1, 3}	{1, 3}	{1, 3}
82	Pb	{-4, 2, 4}	{2, 4}	{2, 4}	{2, 4}
83	Bi	{-3, 1, 3, 5, 7}	{1, 2, 3, 5}	{3}	{3}
84	Po	{-2, 2, 4, 5, 6}	{}	{-2, 2, 4}	{}
85	At	{-1, 1, 3, 5, 7}	{}	{-1, 1}	{}
86	Rn	{2, 6}	{}	{}	{}

Table A.9: The List of oxidation numbers from Francium (Fr) to Californium (Cf)

Z	Elm	smact	icsd	common	Ours
87	Fr	{1}	{}	{1}	{}
88	Ra	{2}	{}	{2}	{}
89	Ac	{2, 3}	{}	{3}	{}
90	Th	{2, 3, 4}	{4}	{4}	{4}
91	Pa	{2, 3, 4, 5}	{}	{5}	{}
92	U	{2, 3, 4, 5, 6}	{3, 4, 5, 6}	{6}	{6}
93	Np	{3, 4, 5, 6, 7}	{}	{5}	{}
94	Pu	{2, 3, 4, 5, 6, 7, 8}	{}	{4}	{}
95	Am	{2, 3, 4, 5, 6, 7}	{}	{3}	{}
96	Cm	{2, 3, 4, 6, 8}	{}	{3}	{}
97	Bk	{2, 3, 4}	{}	{3}	{}
98	Cf	{2, 3, 4}	{}	{3}	{}

A.10 ACCURACTE BAND GAP OPTIMIZATION

We experimented with how precisely the band gap could be optimized. Here, we optimized the band gap to approximately 2.0, regardless of the crystal structure, and simultaneously minimized the formation energy. We conducted all methods in the same manner as mentioned in Section A.6. The results are shown in Table A.10.

Table A.10: Experiments with varying tolerance ranges for band gap optimization. The overall success rate is indicated by the probability of simultaneously satisfying three conditions: (A) the band gap is optimized within the target range, (B) the formation energy is below -0.5 eV, and (C) the crystal structure is valid. C is achieved when two criteria are met simultaneously: (a) all interatomic distances are greater than 0.5 Å, and (b) the structure is electrically neutral. S(Cry) and S(ALI) denote SMOACS utilizing the Crystalformer and ALIGNN models, respectively. We evaluate each of the proposed materials using all evaluation metrics, and the results are averaged over 512 samples.

Target BG (eV)	method	success rate	(A)BG	(B) E_f	(C)STR	(a) neut	(b) 0.5Å
2.00 ± 0.01	S(Cry)	0.234	0.355	0.594	0.781	0.984	0.781
	S(ALI)	0.010	0.012	0.811	0.830	0.910	0.830
	TPE	0.004	0.422	0.053	0.045	0.047	0.777
	FTCP	0.000	0.000	1.000	0.652	0.668	0.924
2.00 ± 0.02	S(Cry)	0.230	0.340	0.543	0.742	0.977	0.742
	S(ALI)	0.037	0.043	0.795	0.803	0.893	0.803
	TPE	0.008	0.623	0.074	0.074	0.074	0.824
	FTCP	0.000	0.000	1.000	0.617	0.652	0.861
2.00 ± 0.04	S(Cry)	0.277	0.418	0.566	0.738	0.984	0.738
	S(ALI)	0.082	0.092	0.820	0.838	0.914	0.838
	TPE	0.016	0.812	0.074	0.061	0.061	0.801
	FTCP	0.004	0.004	1.000	0.645	0.666	0.900
2.00 ± 0.08	S(Cry)	0.238	0.410	0.562	0.730	0.980	0.730
	S(ALI)	0.111	0.119	0.816	0.803	0.912	0.803
	TPE	0.049	0.936	0.135	0.123	0.125	0.846
	FTCP	0.006	0.010	1.000	0.688	0.705	0.928
2.00 ± 0.16	S(Cry)	0.316	0.516	0.570	0.750	0.988	0.750
	S(ALI)	0.193	0.225	0.832	0.820	0.910	0.820
	TPE	0.074	0.955	0.152	0.174	0.186	0.891
	FTCP	0.016	0.027	1.000	0.668	0.695	0.898

1512 A.11 GENERATION OF OXIDATION NUMBER PATTERNS

1513
1514 In SMOACS, realistic oxidation number patterns are generated based on the compositions of
1515 initial crystal structures. Here, we explain this using RuN (mp-1009770). According to
1516 `icsd_oxidation_state` in PyMatGen, ruthenium (Ru) and nitrogen (N) can adopt oxidation
1517 numbers of $\{+2, +3, +4, +5, +6\}$ and $\{+1, +3, +5, -1, -2, -3\}$, respectively. Therefore, elec-
1518 trical neutrality in RuN is achieved when the oxidation number combinations for Ru and N are
1519 $(+2, -2)$ or $(+3, -3)$. Consequently, when using RuN (mp-1009770) as the initial structure, ox-
1520 idation number combination patterns of $(+2, -2)$ and $(+3, -3)$ are obtained, and corresponding
1521 masks are generated for each.

1522 To consider a broader range of oxidation number combinations, we utilized the intersection of ox-
1523 idation numbers from "smact" and "icsd", as listed in Table A.7. It should be noted that even when
1524 generating oxidation number patterns from "smact" and "icsd", electrical neutrality is maintained
1525 by applying site-specific elemental constraints using the oxidation numbers in the "Ours" column of
1526 Table A.7.

1527 A.12 ADJUSTMENT OF PRIORITIES IN THE LOSS FUNCTION

1528
1529 For a fair comparison with TPE, which cannot prioritize each objective, we fixed the value of λ to
1530 1.0 in Equation 14. However, we considered it essential to investigate the effect of λ in optimization
1531 and conducted experiments with various λ values.

1532 The results are shown in Table A.11. These experiments were conducted using SMOACS with
1533 Crystalformer, aiming for a band gap of 2.0 eV and optimizing crystal structures. We found that in-
1534 creasing λ , that is, placing greater emphasis on the formation energy during optimization, improved
1535 the success rate for formation energy. In addition, the probability that all interatomic distances are
1536 greater than 0.5 Å also increased. This is likely because emphasizing formation energy made it
1537 easier to avoid situations where atoms are too close together.

1538
1539 Table A.11: Experiments with varying λ for a band gap target of 2.0 eV using SMOACS with
1540 Crystalformer. The overall success rate is indicated by the probability of simultaneously satisfying
1541 three conditions: (A) the band gap is optimized within the target range, (B) the formation energy is
1542 below -0.5 eV, and (C) the crystal structure is valid. Condition C is achieved when the following
1543 two criteria are met simultaneously: (a) all interatomic distances are greater than 0.5 Å, and (b)
1544 the structure is electrically neutral. We evaluate each of the proposed materials using all evaluation
1545 metrics, and the results are averaged over 128 samples.

λ	success rate	(A)BG	(B) E_f	(C)STR	(a) neut	(b) 0.5Å
0.040	0.086	0.492	0.164	0.617	0.945	0.617
0.200	0.188	0.477	0.328	0.656	0.984	0.656
1.000	0.336	0.453	0.727	0.852	1.000	0.852
5.000	0.266	0.320	0.836	0.875	0.992	0.875
25.000	0.086	0.102	0.859	0.875	1.000	0.875

1554 A.13 EXPERIMENTS WITH MODELS TRAINED ON OTHER DATASETS

1555
1556 We investigated whether optimization is feasible using models trained on datasets other than the
1557 MEGNet dataset. We used ALIGNN models on JARVIS dataset (Choudhary, 2021). The first
1558 experiment employed ALIGNN trained on the JARVIS DFT dataset. The second experiment utilized
1559 ALIGNN trained on the superconductivity dataset, SuperCon. In the first experiment using the
1560 JARVIS DFT data, we utilized models predicting the energy difference from the convex hull⁴ and
1561 the bulk modulus⁵. The crystal structures were optimized to minimize the energy difference from the
1562

1563 ⁴[https://figshare.com/articles/dataset/ALIGNN_models_on_JARVIS-DFT_](https://figshare.com/articles/dataset/ALIGNN_models_on_JARVIS-DFT_dataset/17005681?file=31458658)
1564 [dataset/17005681?file=31458658](https://figshare.com/articles/dataset/ALIGNN_models_on_JARVIS-DFT_dataset/17005681?file=31458658)

1565 ⁵[https://figshare.com/articles/dataset/ALIGNN_models_on_JARVIS-DFT_](https://figshare.com/articles/dataset/ALIGNN_models_on_JARVIS-DFT_dataset/17005681?file=31458649)
[dataset/17005681?file=31458649](https://figshare.com/articles/dataset/ALIGNN_models_on_JARVIS-DFT_dataset/17005681?file=31458649)

convex hull less than 0.5 eV while achieving the bulk modulus within the target range. The results are shown in Tables A.12 and A.13. Similar to the experiments conducted with models trained on the MEGNet dataset in the main text, optimizations using models trained on the JARVIS DFT data were successful. In the second experiment, we employed ALIGNN trained on the SuperCon dataset to predict the critical temperature (T_c)⁶. Since there is no formation energy prediction model trained on the superconductor dataset in JARVIS, we used the formation energy prediction model from the main text. Using these models, we optimized the crystal structures to maximize T_c above a certain temperature while minimizing the formation energy less than -0.5 eV. Specifically, the target temperatures for T_c were set to exceed the 0.901 and 0.963 quantiles of T_c within the dataset, corresponding to temperatures of 10 K and 15 K, respectively. The results are shown in Tables A.14. As with the experiments using models trained on the MEGNet dataset, optimization with models trained on the SuperCon data were successful.

Table A.12: Experiments for various bulk modulus using SMOACS with ALIGNN. The overall success rate is indicated by the probability of simultaneously satisfying three conditions: (A) the bulk modulus is optimized within the target range, (B) the energy difference from the convex hull less than 0.5 eV, and (C) the crystal structure is valid. Condition C is achieved when the following two criteria are met simultaneously: (a) all interatomic distances are greater than 0.5 Å, and (b) the structure is electrically neutral. We evaluate each of the proposed materials using all evaluation metrics, and the results are averaged over 512 samples.

Target Bulk Modulus (GPa)	success rate	(A)BM	(B) E_{hull}	(C)STR	(a) neut	(b) 0.5Å
50.0 ± 5.0	0.020	0.090	0.123	0.512	0.578	0.512
75.0 ± 5.0	0.021	0.082	0.078	0.438	0.535	0.439
100.0 ± 5.0	0.016	0.102	0.066	0.395	0.510	0.395

Table A.13: Experiments for various bulk modulus while preserving perovskite structures using SMOACS with ALIGNN. The overall success rate is indicated by the probability of simultaneously satisfying three conditions: (A) the bulk modulus is optimized within the target range, (B) the energy difference from the convex hull less than 0.5 eV, (C) the crystal structure is valid, and (D) approximating a valid perovskite structure. Criteria (A), (B), and (C) are consistent with those outlined in Table A.12. The Criteria (D) is consistent with that outlined in Table 3. We evaluate each of the proposed materials using all evaluation metrics, and the results are averaged over 512 samples.

Target Bulk Modulus (GPa)	success rate	(A)BM	(B) E_{hull}	(C)STR	(a) neut	(b) 0.5Å	(D)PS	(c) tole	(d) angles	(e) coord
50.0 ± 5.0	0.072	0.309	0.326	0.939	1.000	0.939	0.525	0.525	1.000	1.000
75.0 ± 5.0	0.043	0.271	0.252	0.910	1.000	0.910	0.449	0.449	1.000	1.000
100.0 ± 5.0	0.020	0.178	0.176	0.928	1.000	0.928	0.416	0.416	1.000	1.000

Table A.14: Experiments for various T_c targets using SMOACS with ALIGNN. The overall success rate is indicated by the probability of simultaneously satisfying three conditions: (A) the T_c is optimized within the target range, (B) the formation energy is below -0.5 eV, and (C) the crystal structure is valid. Criteria C is consistent with that outlined in Table A.12. We evaluate each of the proposed materials using all evaluation metrics, and the results are averaged over 512 samples.

Target T_c (K)	success rate	(A) T_c	(B) E_f	(C)STR	(a) neut	(b) 0.5Å
>10.0	0.049	0.121	0.625	0.656	0.875	0.656
>15.0	0.004	0.039	0.604	0.693	0.906	0.693

⁶https://figshare.com/articles/dataset/ALIGNN_models_on_JARVIS-DFT_dataset/17005681?file=38789199

A.14 OPTIMIZATION WITH MARGINS BASED ON PREDICTOR ERROR

To ensure a fair comparison of optimization methods, we fixed the margin for all band gaps at 0.04 eV in the main text. However, in practical applications, it is conceivable to set the margin based on the predictor’s prediction error. Here, we present the optimization results when the predictor’s errors shown in Table 1 are used as margins. We performed optimizations regardless crystal structure and optimizations with preserving the perovskite structure, using the hyperparameters described in Sections A.5 and A.7, respectively. The results are shown in Tables A.15 and A.16. As shown in these Tables, FTCP has low expected values for satisfying the band gap value and maintaining the perovskite structure, and TPE has a low expected value for satisfying the formation energy; therefore, SMOACS has achieved the best results.

Table A.15: Experiments on optimizing for various targets of a band gap. We adopted the error values of each predictor in Table 1 as the margin for the band gap. The entries Cry, ALI, and F-Reg in the Predictor column correspond to the Crystalformer, ALIGNN, and regression branches of FTCP, respectively. Evaluation methods are based on those described in Table A.2.

Target BG (eV)	method	Predictor	success rate	(A)BG	(B) E_f	(C)STR	(a) neut	(b) 0.5Å
0.50±0.20	S(Cry)	Cry	0.410	0.598	0.637	0.754	0.961	0.754
0.50±0.22	S(ALI)	ALI	0.336	0.387	0.855	0.867	0.941	0.867
0.50±0.20	TPE	Cry	0.109	1.000	0.289	0.305	0.336	0.945
0.50±0.44	FTCP	F-Reg	0.059	0.117	1.000	0.695	0.719	0.867
1.50±0.20	S(Cry)	Cry	0.504	0.645	0.727	0.828	0.984	0.828
1.50±0.22	S(ALI)	ALI	0.227	0.262	0.848	0.836	0.918	0.836
1.50±0.20	TPE	Cry	0.117	1.000	0.219	0.273	0.312	0.898
1.50±0.44	FTCP	F-Reg	0.039	0.039	1.000	0.695	0.727	0.875
2.50±0.20	S(Cry)	Cry	0.391	0.527	0.734	0.797	0.996	0.797
2.50±0.22	S(ALI)	ALI	0.238	0.270	0.844	0.781	0.914	0.781
2.50±0.20	TPE	Cry	0.062	0.961	0.148	0.172	0.188	0.891
2.50±0.44	FTCP	F-Reg	0.066	0.094	1.000	0.703	0.734	0.895

Table A.16: Experiments optimizing for various band gaps and while preserving a perovskite structure. We adopted the error values of each predictor in Table 1 as the margin for the band gap. The entries Cry, ALI, and F-Reg in the Predictor column correspond to the Crystalformer, ALIGNN, and regression branches of FTCP, respectively. Evaluation methods are based on those described in Table A.4.

Target BG (eV)	method	Predictor	success rate	(A)BG	(B) E_f	(C)STR	(a) neut	(b) 0.5Å	(D)PS	(c) tole	(d) angles	(e) coord
0.50±0.20	S(Cry)	Cry	0.145	0.516	0.465	0.957	1.000	0.957	0.512	0.512	1.000	1.000
0.50±0.22	S(ALI)	ALI	0.191	0.516	0.473	1.000	1.000	1.000	0.449	0.449	1.000	1.000
0.50±0.20	TPE	Cry	0.039	1.000	0.492	0.914	0.914	1.000	0.258	0.258	1.000	1.000
0.50±0.44	FTCP	F-Reg	0.078	0.363	1.000	0.883	0.898	0.965	0.234	0.551	0.465	0.266
1.50±0.20	S(Cry)	Cry	0.227	0.566	0.527	0.980	1.000	0.980	0.594	0.594	1.000	1.000
1.50±0.22	S(ALI)	ALI	0.234	0.473	0.875	1.000	1.000	1.000	0.570	0.570	1.000	1.000
1.50±0.20	TPE	Cry	0.070	1.000	0.484	0.773	0.773	1.000	0.289	0.289	1.000	1.000
1.50±0.44	FTCP	F-Reg	0.039	0.129	1.000	0.867	0.883	0.961	0.258	0.531	0.465	0.281
2.50±0.20	S(Cry)	Cry	0.188	0.363	0.551	0.992	1.000	0.992	0.621	0.621	1.000	1.000
2.50±0.22	S(ALI)	ALI	0.238	0.379	0.961	1.000	1.000	1.000	0.641	0.641	1.000	1.000
2.50±0.20	TPE	Cry	0.062	1.000	0.508	0.656	0.656	1.000	0.320	0.320	1.000	1.000
2.50±0.44	FTCP	F-Reg	0.062	0.148	0.992	0.883	0.891	0.957	0.219	0.543	0.422	0.273